# Studies on analysis of acoustic fields generated by flexural wave propagating on flat panel and its applications

March 2016

Ayaka Fujii

# Studies on analysis of acoustic fields generated by flexural wave propagating on flat panel and its applications

Graduate School of Systems and Information Engineering
University of Tsukuba

March 2016

Ayaka Fujii

# Abstract

This paper aims to analyze the characteristics of the flexural wave propagation and the acoustic fields generated by the flexural wave suitable for objective applications. The flexural wave and the generated acoustic fields have been analyzed using various experiments and calculations. However, there were few applications using the acoustic fields those were generated by flexural waves with a wide frequency band in audible frequency. Therefore, this study aims to excite the flexural wave in audio frequency, analyze the generated acoustic fields, and propose applications using the characteristics of the acoustic fields.

The dispersions of the phase velocities of the flexural waves in the homogeneous panel and the sandwich panel are different from each other. In the case of the homogeneous panel, the phase velocity that obtained using the motion equation of the beam was determined as the theoretical value. A planar transducer that consists of acrylic plastic plate was designed to measure the phase velocity of the flexural wave. It was confirmed that the experimental values were in good agreement with the theoretical values. In the case of the honeycomb sandwich panel, the method of the calculation of the phase velocity of the flexural wave was proposed. The theoretical value of the phase velocity was obtained using a plate equation by combining the full equation of motion for elastic material and constitutive relations. The elastic constants of a honeycomb core layer were calculated using the shape and the physical property of the honeycomb cell to substitute into the theoretical equation. In addition, the phase velocity of the flexural wave was measured using the honeycomb sandwich panel made of aluminum to compare among the theoretical value, the simulated value, and the experimental value. The simulated value was well-accorded with the theoretical value. On the other hand, the gap between the theoretical value and the experimental value was caused due to the effect of the mass of the adhesive layer. However, it was indicated that the behavior of the honeycomb sandwich panel that has complex structure can be predicted easily using the proposed method. Using these knowledge, the acoustic transducer that generates the inclined sound and the evanescent sound field is designed by the calculation of the characteristics of the flexural wave.

A flat panel loudspeaker using inclined sound for generating guiding sound was proposed. The inclined sound is radiated in air when the phase velocity of the flexural wave is larger than the sound velocity in air. The honeycomb sandwich panel was designed for generating inclined sound by changing the core height and the cell size in honeycomb structure. It was found that the phase velocity and the group velocity of the flexural wave increased rapidly at low frequency with increasing the core height so that the sound field became non-evanescent. In addition, the phase velocity becomes almost non-dispersive at low frequency with increasing the cell size. The sound radiation from the designed panel was simulated using FEM. It was confirmed that the characteristic of radiating sound with uniform angle is useful for indicating the direction of the destination. The obtained results suggested that the proposed loudspeaker using a honeycomb sandwich panel is suitable for audio guidance systems.

A planar acoustic transducer generating the evanescent sound field for near-field acoustic communication was proposed. We attempt to generate the evanescent wave in audio frequency with large level so that mobile devices equipped with microphones can be receive the acoustic data. The distribution of sound pressure level of the sound field above the acoustic transducer was evaluated by means of a simulation and an experiment. The obtained results suggest that the proposed acoustic transducer can generate the

evanescent wave because amplitude of sound pressure was attenuated exponentially. In addition, it was clarified that acoustic data can be received near the plate by mobile device since sound is generated with uniform level from all over the surface and small time delay. However, it was found that attenuation of sound pressure becomes small because of the sound leakage from the evanescent sound field. Therefore, a method of suppressing sound leakage to the far field of a near-field acoustic communication system using an evanescent sound field was proposed. A sound wave leaks slightly over an evanescent sound field because of the broadening of the wavenumber spectrum caused by the presence of a discontinuity in the particle velocity distribution. Therefore, we calculated an optimal window function, which performs spatially-weighting the particle velocity field near a vibrating plate, in order to suppress sound leakage. It was confirmed that the optimized window function can limit the area in which acoustic data is transmitted while securing high sound pressure level near the vibrating plate. Additionally, it was found by simulation using the three-dimensional FEM that sound radiation can be suppressed by placing a sound insulator made of porous material, which has a spatially-weighted shape as the optimized window, above the vibrating surface. Therefore, the applicability of the realization of near-field acoustic communication system using the proposed acoustic transducer was indicated.

These results provides the valuable knowledge for the multiple areas of analyzing and utilizing of the flexural wave and the acoustic fields.

# Contents

# List of Figures

# List of symbols

**General:**

| | |
|---|---|
| $x$ | Rectangular coordinates in longitudinal direction of panel |
| $y$ | Rectangular coordinates in cross direction of panel |
| $z$ | Rectangular coordinates in thickness direction |

**Vibration quantities:**

| | |
|---|---|
| $\omega$ | Angular frequency |
| $f$ | Frequency |
| $c$ | Sound velocity of plane wave in air |
| $\lambda$ | Wavelength of plane wave in air |
| $\boldsymbol{k}$ | Wavenumber of plane wave in air |
| $k_x$ and $k_z$ | Components in $x$- and $z$-directions |
| $\phi$ | Velocity potential |
| $p$ | Sound pressure |
| $v_\mathrm{p}$ | Phase velocity of flexural wave in panel |
| $v_\mathrm{g}$ | Group velocity of flexural wave in panel |
| $\lambda_\mathrm{p}$ | Wavelength of flexural wave in panel |
| $k_\mathrm{p}$ | Wavenumber of flexural wave in panel |

**Panel quantities:**

| | |
|---|---|
| $E$ | Young's modulus |
| $G$ | Modulus of rigidity |
| $\rho$ | Density |
| $\nu$ | Poisson's ratio |
| $\kappa$ | Radius of gyration on bending deformation |
| $u$ | Displacement of homogeneous panel in $z$-direction |
| $\tilde{u}$ | Complex amplitude of displacement $u$ |
| $d$ | Thickness of panel |
| $L$ | Length of panel |
| $W$ | Width of panel |
| $t_\mathrm{f}$ | Thickness of face plate of honeycomb sandwich panel |

| | |
|---|---|
| $t_{\mathrm{a}}$ | Thickness of adhesive layer of honeycomb sandwich panel |
| $h$ | Core height of honeycomb sandwich panel |
| $n$ | Total number of layers in sandwich panel |
| $w$ | Displacement of sandwich panel in $z$-directionl |
| $\psi$ | Cross section angle of sandwich panel makes with $z$-axis |
| $D$ | Stiffness of flexural deformation |
| $K$ | Stiffness of shearing deformation |
| $I$ | Rotary inertia |
| $M$ | Mass |
| $c_{ij}$ | Elastic stiffness |
| $l_i$ | Length between natural plane and panel surface of each |
| $N$ | Number of half wavelengths in panel |
| $\omega_{\mathrm{TS}}$ | Natural frequency of fundamental thickness-shear mode |
| $Z_i$ | Impedance |
| $R_i$ | Characteristic impedance |
| $\gamma_i$ | Wavenumber of shear wave |
| $a$ | Wall thickness of honeycomb cell |
| $s$ | Size of honeycomb cell |

**Piezoelectric ceramics quantities:**

| | |
|---|---|
| $c_{ij}^{E}$ | Elastic stiffness ($E = 0$) |
| $e_{ij}$ | Piezoelectric stress constant |
| $\epsilon_{ij}^{S}$ | Relative permittivity ($S = 0$) |

**Communication quality:**

| | |
|---|---|
| $T_{\mathrm{g}}$ | Group delay time |
| $\tau$ | Maximum tolerable delay time difference |
| $p_{\mathrm{e}}$ | Bit error rate |
| $E_{\mathrm{b}}/N_0$ | Energy per bit to noise power spactral density ratio |

**Window function:**

| | |
|---|---|
| $l$ | Shoulder length of window |
| $L_{\max}$ | Maximum sound pressure level |
| $S$ | Total area of the vibration surface |
| $Z$ | Characteristic impedance |
| $\gamma$ | Propagation constant |
| $R_{\mathrm{f}}$ | Flow resistivity |

# Chapter 1

# Introduction

## 1.1 Background

Lamb wave propagating in elastic solid has been studied as guided wave for non-destructive inspection in the past decades.[1–4] The word guided wave is commonly used in referring to modes of ultrasound propagating on boundaries of a panel and bar in a longitudinal direction. Guided wave is characterized by propagating long distance with small energy dissipation. Therefore, high speed long distance inspection of elongated material such as a pipework and railroad rail is achieved using the characteristics of Lamb wave.

Lamb wave has dispersibility of the phase velocity.[5] Basic researches has been carried out to analyze the frequency characteristics of Lamb wave in detail.[6] Especially, the phenomenon called leaky Lamb wave, whose energy is partly radiated into an adjacent medium, has been received broad attention. This occurs when the phase velocity is larger than the sound velocity in the medium. Non-contact inspection using the leaky Lamb wave has been attempted to evaluate defects of the panel by receiving radiated wave from the leaky Lamb wave.[7] In addition, the radiation pressure has been also utilized in many fields, such as non-contact transportation[8] and ultrasonic cleaning.[9]

In contrast, it is known as interesting phenomenon that the energy from Lamb wave propagating on the panel is localized on nearby surface of the panel when the phase velocity is smaller than the sound velocity in the adjacent medium.[10] The generated wave is called an evanescent wave, especially the field is called an evanescent field. The evanescent wave does not propagate in free space and its magnitude decays exponentially in the direction perpendicular to the boundary surface. The evanescent wave has been particularly studied in the areas of optics and electromagnetics.[11,12] When a light wave (transverse wave) enters an adjacent medium that has low refractive index from a medium that has high refractive index in excess of the critical angle, the light wave reflects totally at the interface. The evanescent wave is generated in the adjacent medium. Total internal reflection fluorescence microscope uses the evanescent wave as lighting for fluorophores.[13] The evanescent wave is suitable for the observation of the phenomenon on nearby surface of the cover slip because fluorophores are excited only in the distance of the wavelength. Using the same principle, the evanescent wave excites surface plasmon resonance and it is utilized for the biosensor.[14] In the area of acoustics, the use of the evanescent sound field is relatively new field of study. For instance, near-field acoustic holography allows high spacial resolution imaging by use of evanescent

component as well as radiating component.[15–17] In addition, a wavenumber-frequency calibrator of sonar array generating the evanescent sound field under water has been proposed to reduce the impact of flow noise on array.[18] This calibrator consists of planar array using a sheet of polyvinylidene difluoride. It has been reported that the electric admittance changes when an object is brought into the evanescent sound field generated at an edge of the vibration panel.[19,20] Therefore, a proximity sensor using the characteristics has been proposed. Furthermore, a loudspeaker system using dipole acoustic transducers and digital filters for generating the evanescent sound field in audio frequency has been studied recently.[21] As stated above, the characteristics of the acoustic fields have been studied with great interest and attempted to create its application.

## 1.2 Objective

Figure 1.1 shows examples of applications using Lamb wave, leaky Lamb wave, and the generated acoustic field. Lamb wave and the generated acoustic fields has been analyzed using various experiment and calculation. However, there were few applications using the acoustic fields with a wide frequency band in the audible frequency. One mode of Lamb wave is assumed as the flexural wave in the case of low frequency, i.e., audio frequency in which the wavelength is larger than the panel thickness. Therefore, this study aims to excite the flexural wave in audio frequency, analyze the generated acoustic fields, and propose applications using the characteristics of the acoustic fields.

In order to design the acoustic transducer for utilize of the acoustic fields, the characteristics of the flexural wave is calculated. The motion of the flexural wave propagating on the homogeneous panel are described using the motion equation of the bar. The frequency characteristics of the phase velocity is analyzed to design an acoustic transducer by comparison between theoretical equation and experiment. On the other hand, the dynamic behavior of the multi-layered panel, such as the honeycomb sandwich panel, has been analyzed by simulation using the three-dimensional (3D) finite element method (FEM) in recent studies.[22,23] There is a problem that the computational effort of the 3D FEM increases owing to the complex structure of the honeycomb sandwich panel. Therefore, the prediction of the behavior of the sandwich panel using a theoretical equation is attractive for optimizing the structure of the panel by varying the parameters such as the thickness of the core layer or the face plate. For the reason, an easily-calculated method to analyze the sandwich panel including the honeycomb sandwich panel is proposed. It will be helpful for the design and adjustment of a loudspeaker if the phase velocity of the flexural wave can be easily calculated using these parameters of the honeycomb sandwich panel.[24]

The plane wave with inclined angle with respect to the panel is radiated when the leaky Lamb wave propagates in one direction. The radiated plane wave is called the inclined plane wave in this paper.[25] The inclined plane wave propagates extensively with uniform level and direction. We aim to apply the inclined plane wave to audio guidance system since the characteristics are attractive to lead pedestrians accurately. From the viewpoint of the application in an audio guidance system, we need to generate the inclined plane wave in a wide-frequency band with a small velocity dispersion so that people can perceive the direction easily. Moreover, the distribution of sound pressure and the direction of sound in a sound field above the proposed loudspeaker are determined in the simulation to identify the inclined plane wave generation.

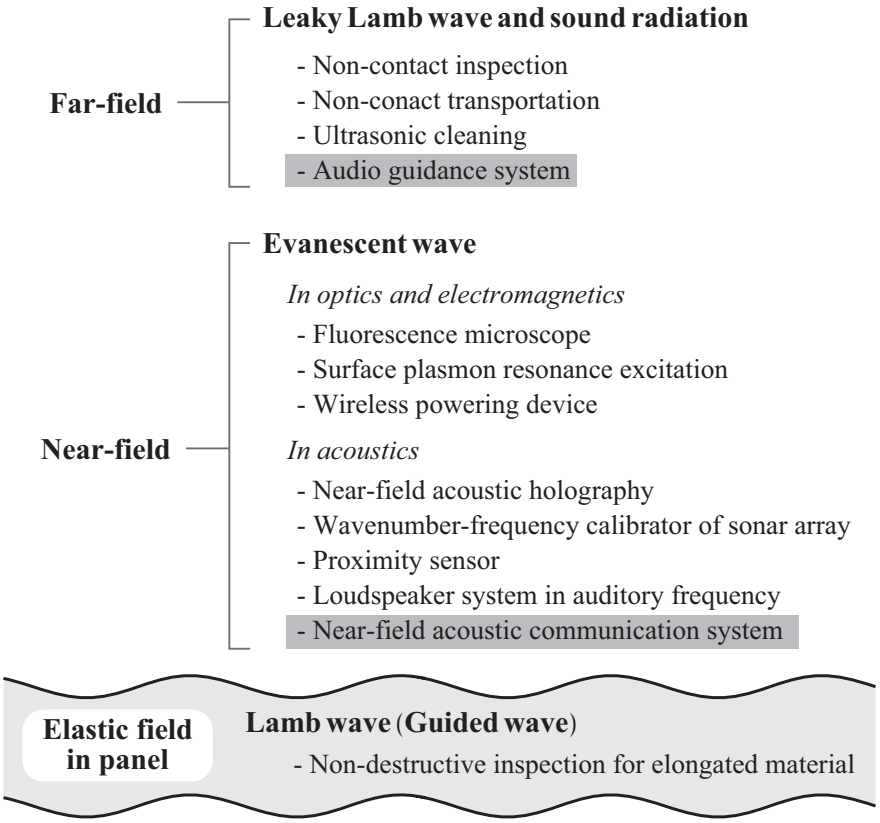


Figure 1.1: Applications using Lamb wave, leaky Lamb wave, and the generated acoustic field.

In addition, near-field acoustic communication system is proposed using the evanescent sound field that can provide the acoustic data only near the surface of the vibration panel.[26] It is confirmed using the simulation and experiment that the receivable area of the acoustic data can be limited to prevent information and noise leakage. Furthermore, a sound insulator made of the porous material is designed to suppress sound leakage to from the evanescent sound field.[27]

## 1.3 Composition of thesis

This paper aims to analyze the characteristics of the elastic wave and its acoustic fields to generate the acoustic fields for objective application. The dispersion of the phase velocity of the flexural wave is different between the homogeneous panel and the sandwich panel. Therefore, the calculation method to analyze the characteristics of the flexural wave propagating on the panel is proposed. In addition, the feasibility of the applications using the inclined plane wave and the evanescent sound field is estimated. The composition and contents of this paper is shown in Fig. 1.2.

In chapter 2, the frequency characteristics of the phase velocity of the flexural wave propagating on homogeneous panel and honeycomb sandwich panel are analyzed. First, the propagation characteristics of the elastic wave, especially Lamb wave, is explained. Next, the motion equation of the beam is indicated as the theoretical equation for the homogeneous panel. The phase velocity of the flexural wave is measured

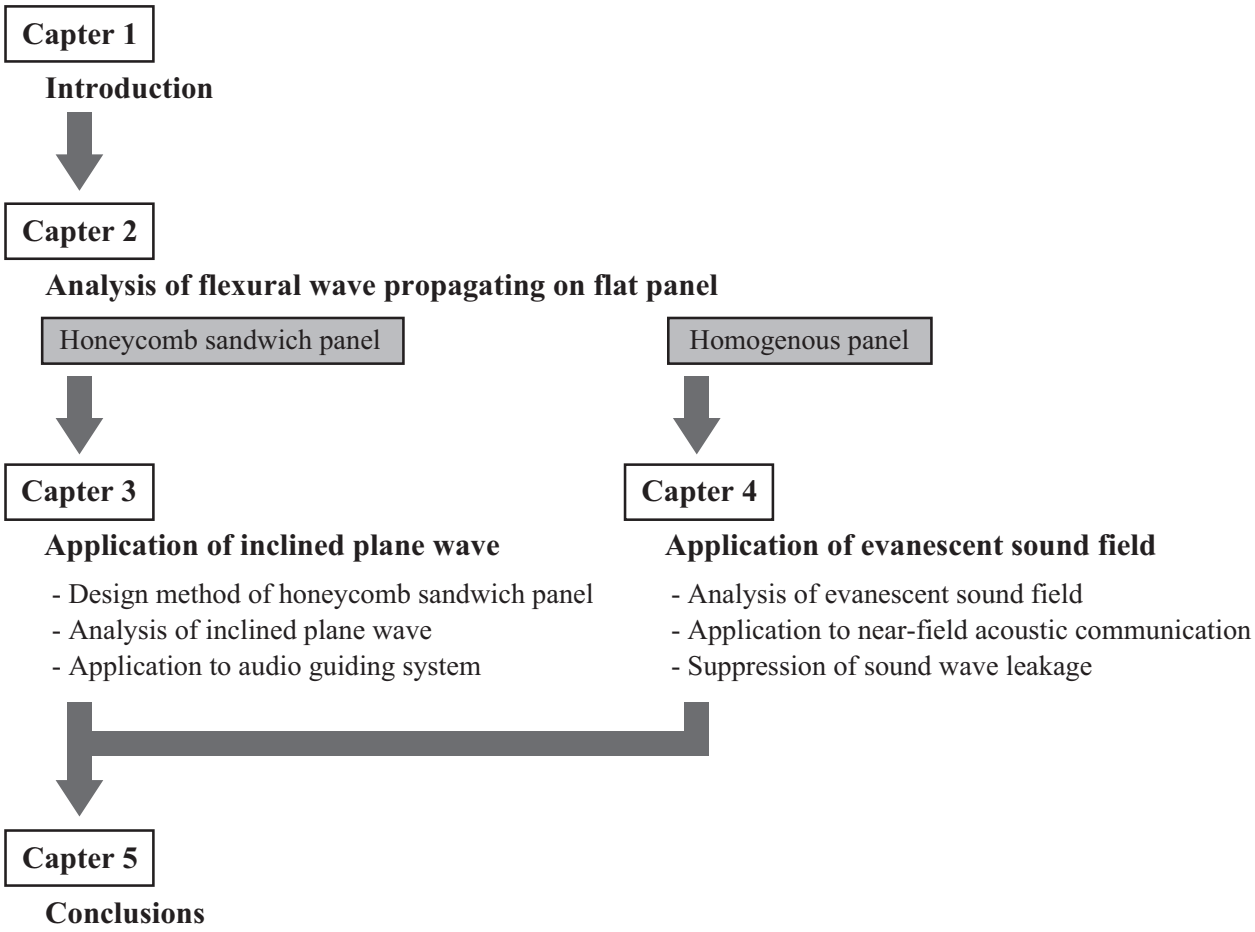


Figure 1.2: Composition and contents of this paper.

using a planar transducer that consists of the acrylic plastic and the piezoelectric transducer, and compared to the theoretical value. Finally, the calculation method of the phase velocity of the flexural wave for the honeycomb sandwich panel is proposed. The applicability of the proposed method for design the honeycomb sandwich panel is confirmed by comparing among the theoretical value, simulated value, and the experimental value.

In chapter 3, a flat panel loudspeaker using inclined plane wave for generating guiding sound is proposed. First, the demand of the audio guidance system and the problem of existing system is mentioned. Next, the principle of generating inclined plane wave by the flexural wave is indicated. Using the proposed calculation method in chapter 2, the honeycomb sandwich panel for generating inclined plane wave is designed. The sound radiation from the designed panel is simulated using FEM. The angle of radiated sound from the honeycomb sandwich panel is calculated to show the suitability of the proposed loudspeaker as an audio guidance systems.

In chapter 4, a planar acoustic transducer generating the evanescent sound field for near-field acoustic communication is proposed. First, the background of the near-field communication system and the existing application using the evanescent sound field is mentioned. Next, generation of the evanescent sound field

is confirmed by FEM simulation and the experiment. The communication quality of the proposed acoustic transducer is estimated. It was found that a sound wave radiates over an evanescent sound field because of the broadening of the wavenumber spectrum caused by the presence of a discontinuity in the particle velocity. Therefore, in order to suppress sound leakage, we calculate an optimum window function applying to the particle velocity field near a vibrating plate. We investigate a suitable method for calculating the sound pressure level at the far field, and the sound pressure level at the far field with respect to the frequency was calculated for different window shapes. In addition, leaking sound is suppressed using sound insulator made of a porous material in FEM simulation. The applicability of the realization of near-field acoustic communication system using the proposed acoustic transducer is indicated.

Chapter 5 is conclusions of this thesis.

# Chapter 2

# Analysis of flexural wave propagating on flat panel

## 2.1 Characteristics of flexural wave propagating on flat elastic panel

Lamb wave is a type of elastic wave propagating on a elastic panel with thickness comparable to its wavelength. The displacement of the panel surface is symmetric or antisymmetric with respect to the central plane. These vibration modes are called symmetric mode and antisymmetric mode, such as $S_0$-mode, $A_0$-mode, and their higher order modes. Here, Fig. 2.1 shows the dispersion curves of the phase velocity of aluminum (5754 H-22). There are multiple modes that have different phase velocity dispersions. The phase velocity vary greatly depending on frequency, i.e., the phase velocity has high dispersivity. Figure 2.1(a)–(d) show the displacement distribution of $S_0$-mode, $S_1$-mode, $A_0$-mode, and $A_1$-mode. At low frequency in which the wavelength is larger than the thickness of the panel, $A_0$-mode Lamb wave on thin panel is assumed as flexural wave.

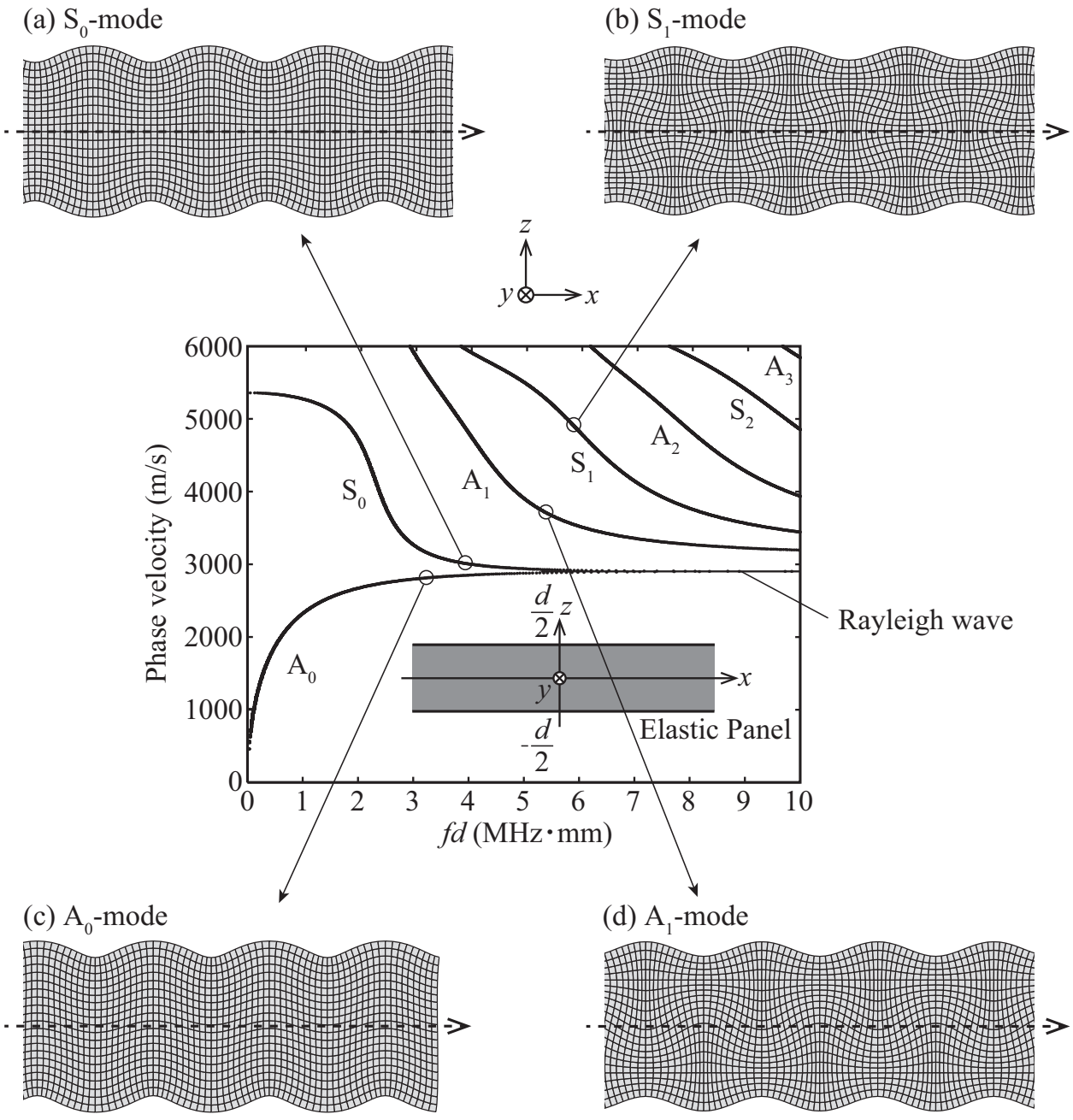


Figure 2.1: Dispersion curves of the phase velocity of aluminum (5754 H-22) and displacement distribution of Lamb wave, (a) $S_0$-mode, (b) $S_1$-mode, (c) $A_0$-mode, and (d) $A_1$-mode.

## 2.2 Analysis of phase velocity of flexural wave propagating on homogeneous panel

### 2.2.1 Calculation of phase velocity of flexural wave propagating on homogeneous panel

Flexural vibration is expressed as beam vibration. The motion of elastic beam is given as following equation.

$$\rho \frac{\partial^2 u}{\partial t^2} = -E\kappa^2 \frac{\partial^4 u}{\partial x^4}, \tag{2.1}$$

where $u$ is displacement in the $z$-direction, as shown in Fig. 2.1. The density and Young's modulus is expressed as $\rho$ and $E$. For the thickness of the beam $d$, radius of gyration is expressed as $\kappa = d/\sqrt{12}$. Here, general solution of Eq. (2.1) is expressed as sine wave as following equation.

$$u(x) = \tilde{u} \exp\left[j(\omega t - k_{\mathrm{p}} x)\right], \tag{2.2}$$

where $\tilde{u}$, $\omega$, and $k_{\mathrm{p}}$ are complex amplitude, angular frequency, and wavenumber of beam in the $x$-direction. There exists a relation among phase velocity of the flexural wave $v_{\mathrm{p}}$, $\omega$, and $k_{\mathrm{p}}$ as follows; $\omega = k_{\mathrm{p}} v_{\mathrm{p}}$. By substituting Eq. (2.2) into Eq. (2.1), $v_{\mathrm{p}}$ is obtained.

$$v_{\mathrm{p}} = \left(\omega^2 \frac{E\kappa^2}{\rho}\right)^{\frac{1}{4}}, \tag{2.3}$$

It can be seen that $v_{\mathrm{p}}$ is proportional to the square root of frequency, i.e. has frequency dispersion.

Here, we take an acrylic plastic panel (Mitsubishi Rayon SHINKOLITE) as an example. The density and Young's modulus of the panel are 1,225 kg/m$^3$ and 5.613 GPa, respectively. Figure 2.2 shows the frequency characteristics of the phase velocity and the wavelength of the flexural wave propagating in acrylic plastic with the thickness of 2 mm, which are calculated using Eq. (2.3). The left vertical axis and solid line show the phase velocity of the flexural wave, and the right vertical axis and dotted line show the wavelength of the flexural wave, respectively. According to Fig. 2.2, when sound velocity in air is 340 m/s, the phase velocity of the flexural wave whose frequency is under 15 kHz is slower than the sound velocity. Then sound does not propagate from infinite panel, and the evanescent sound field is locally generated in theory. In order to confirm that the frequency characteristics of the phase velocity of the flexural wave propagating on the finite homogeneous plate, we design a planar acoustic transducer, and examine the phase velocity.

### 2.2.2 Measurement of phase velocity

A planar transducer was designed to measure the phase velocity of the flexural wave. Figure 2.3 shows the shape of a planar acoustic transducer and a position of a probe microphone on the $xz$-axes PC controlled stage. This transducer consists of acrylic plastic plate (vibration plate) and piezoelectric ceramic transducers (vibration source). The width of the piezoelectric ceramic transducers was assumed as mirror symmetry at edge of the plate since flexural wave reflects at edge of the plate. Widths of the piezoelectric ceramic transducers were 7.5 mm, which is 1/4 of wavelength of the flexural wave at 10 kHz frequency as shown

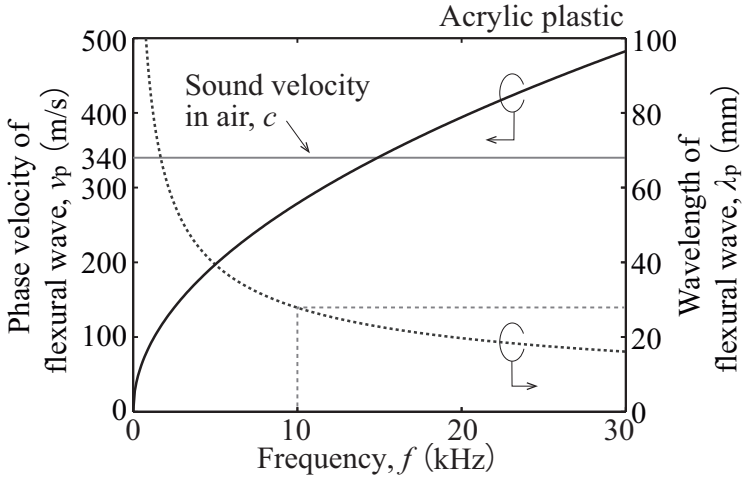


Figure 2.2: Frequency characteristics of phase velocity and wavelength of the flexural wave propagating in acrylic plastic with the thickness of 2 mm.

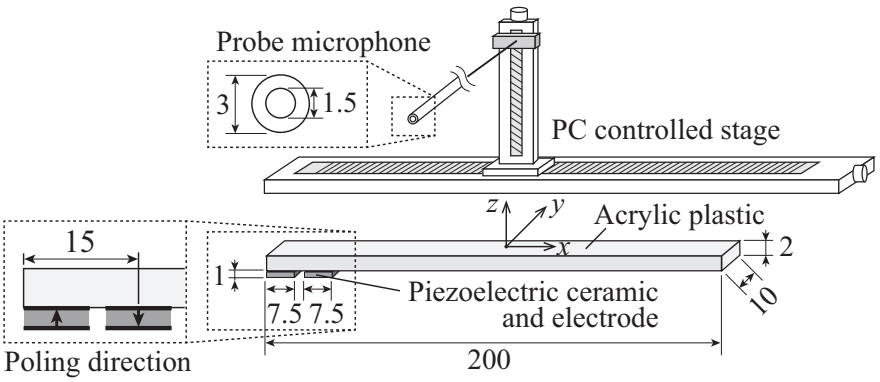


Figure 2.3: Shape of a planar acoustic transducer and a position of a probe microphone on the $x$- and $z$-axes PC controlled stage.

in Fig. 2.3. Young's modulus and Poisson's ratio of acrylic plastic were 5.613 GPa and 0.32, respectively. Table 2.1 shows elastic stiffness $c$, piezoelectric stress constant $e$, and relative permittivity $\varepsilon$ of piezoelectric ceramic transducers (Fuji Ceramics C-213).

We used a probe microphone whose bore was enough smaller than wavelength of sound to avoid effect of reflection on the sound field. The probe microphone was scanned to calculate received signal at each point. The center and the surface of panel was defined as the origin of the $xz$-coordinates as shown in Fig. 2.3. The probe microphone was scanned between $-150 \leq x \leq 150$ mm for every 1 mm. The microphone was maintained under 5 mm distance from the surface of the panel. Time stretched pulse (TSP) signal was used as driving signal, and the impulse response of the acoustic transducer at each receive point was obtained. The number of sampling of TSP signal was 65,536, and the amplitude of TSP signal was 10 V. Received signal by the probe microphone was sampled at 100 kHz by Analog-Digital converter (NI USB-6212).

Table 2.1: Material constants of C-213.

| Elastic stiffness (GPa) | |
|---|---|
| $c_{11}^E$ | 138.9 |
| $c_{12}^E$ | 77.8 |
| $c_{13}^E$ | 74.3 |
| $c_{33}^E$ | 115.4 |
| $c_{44}^E$ | 25.6 |
| $c_{66}^E$ | 30.6 |

| Piezoelectric $e$ stress constant (C/m$^2$) | |
|---|---|
| $e_{31}$ | -5.2 |
| $e_{33}$ | 15.1 |
| $e_{15}$ | 12.7 |

| Relative permittivity | |
|---|---|
| $\varepsilon_{11}^S$ | 762.5 |
| $\varepsilon_{33}^S$ | 664.2 |

### 2.2.3 Results and discussions

The phase velocity of the flexural wave on the panel was calculated. Sound pressure with respect to each frequency at each receive point was found using the transfer function obtained by computing the discrete Fourier transform of the impulse response. The spatial frequency spectrum with respect to each frequency was calculated by computing the discrete Fourier transform of complex amplitude distribution of sound pressure on the $x$-coordinate. The dispersion curve of $v_\mathrm{p}$ with respect to each spatial frequency can be calculated by dividing the frequency by the spatial frequency spectrum; $v_\mathrm{p} = 2\pi f/k_\mathrm{p}$. A wave number spectrum of sound pressure at the surface of the panel was obtained by measured sound pressure in the experimental result. In addition, frequency characteristics of the phase velocity of the flexural wave was calculated by the wavenumber spectrum. Figures 2.4(a) and 2.4(b) show the frequency characteristics of the phase velocity of the flexural wave in cases of the panel without the damper, and with the clay damper attached at the end of the panel, respectively. Normalized power was shown as contrasting density. The power was normalized by the maximum power of each frequency. The solid line shows the theoretical values calculated using Eq. (2.3). The positive and negative directions of the phase velocity follow the $x$-axis in Fig. 2.3.

The phase velocity in the experimental result was well fitted with the theoretical values as shown in Fig. 2.4. Additionally, Fig. 2.4(a) shows that a component of negative direction of the phase velocity existed because the flexural wave reflected at the edge of the panel in the case of the panel without the damper. On the other hand, Fig. 2.4(b) shows that the flexural wave proceeded in a single direction in the case of the panel with the damper. Figures 2.5(a) and 2.5(b) show the phase velocity when driving frequency $f$ was 10 and 20 kHz in cases of the panel without the damper, and with the damper, respectively. The solid line and chain line show the results of $f$ = 10 and 20 kHz, respectively. The circle marks show the theoretical values. The dashed line shows the sound velocity of the plane wave in air (340 m/s). It is confirmed that the phase

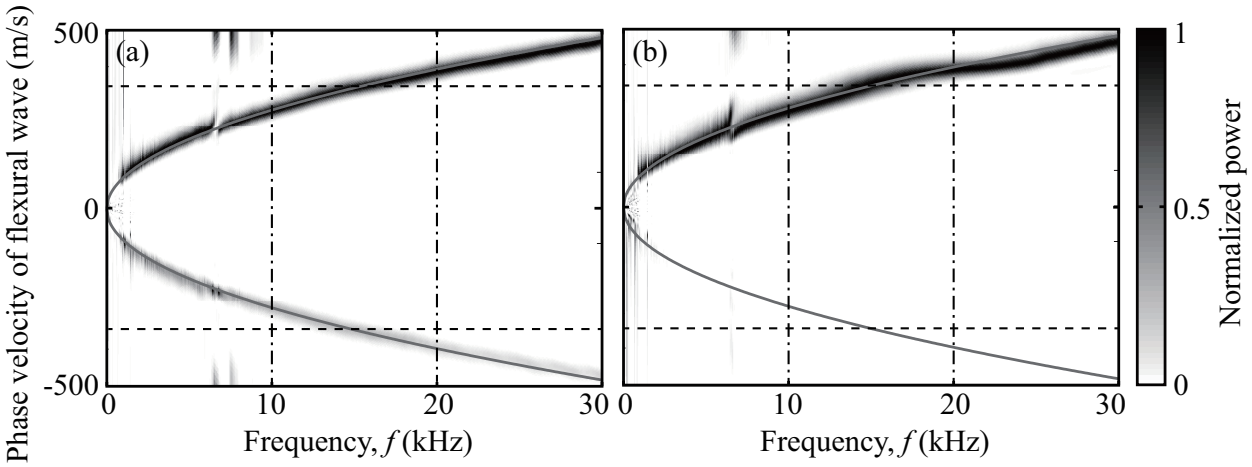


Figure 2.4: Frequency characteristics of phase velocity of theoretical values and experimental values: (a) the plate without damper and (b) the plate with damper.

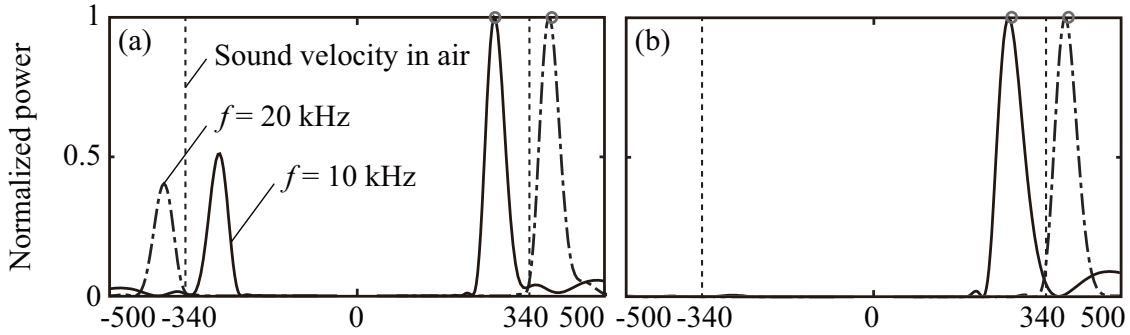


Figure 2.5: Phase velocity of theoretical values and experimental values: (a) the plate without damper and (b) the plate with damper.

velocity of the flexural wave was slower than sound velocity in air when $f$ = 10 kHz. On the other hand, the phase velocity was faster than the sound velocity in air when $f$ = 20 kHz. According to these results, it was substantiated that the phase velocity of the flexural wave with respect to the sound velocity in air can be analyzed using the motion equation of the beam. In other words, the vibration panel for the application using the acoustic fields can be designed by calculating the condition under which the evanescent sound field or the inclined plane wave is generated.

## 2.3 Analysis of phase velocity of flexural wave propagating on honeycomb sandwich panel

### 2.3.1 Calculation of phase velocity of flexural wave propagating on honeycomb sandwich panel

The calculation method of the phase velocity of the flexural wave is proposed to analyze the behavior of a honeycomb sandwich panel. Here, we provide the following methods that are used to establish the theoretical equation.

**Plate theory** Figure 2.6 shows the structures of honeycomb sandwich panels. The sandwich panel that is modeled by a five-layered structure composed of two face panels, two adhesive layers, and a core layer, as shown in Fig. 2.6(a). The sandwich panel can be treated as a three-layered structure when the dynamic behavior of the panel is analyzed when the adhesive layers are very thin, as shown in Fig. 2.6(b). In that case, the thickness of the adhesive layer is ignored, and the adhesive layer and the face panel are considered as a single panel whose weight and stiffness are a combination of those of the face panel and the adhesive layer. Thompson et al. have developed a plate equation by combining the full equation of motion of for elastic material and constitutive relations:[28)]

$$D\frac{\partial^2\psi}{\partial x^2} - K\left(\psi + \frac{\partial w}{\partial x}\right) = I\frac{\partial^2\psi}{\partial t^2}, \tag{2.4}$$

$$K\left(\frac{\partial\psi}{\partial x} + \frac{\partial^2\psi}{\partial x^2}\right) = M\frac{\partial^2 w}{\partial t^2}. \tag{2.5}$$

Here, $w$ is the displacement of the panel normal to its face and $\psi$ is the angle that a cross section of the panel makes with respect to the $z$-axis:

$$D = \frac{2}{3}\sum_{i=1}^{n}\left(c_{11} - \frac{c_{13}c_{31}}{c_{33}}\right)_i\left(l_i^3 - l_{i+1}^3\right), \tag{2.6}$$

$$K = I\omega_{\mathrm{TS}}^2, \tag{2.7}$$

$$I = \frac{2}{3}\sum_{i=1}^{n}\left(l_i^3 - l_{i+1}^3\right), \tag{2.8}$$

$$M = 2\sum_{i=1}^{n}\rho_i\left(l_i - l_{i+1}\right), \tag{2.9}$$

where $D$ and $K$ are the stiffnesses of the flexural and shearing deformations, respectively. The elastic constants of the honeycomb core are expressed as $c_{11}$, $c_{13}$, $c_{31}$, and $c_{33}$, which are given by the physical property of the material and by the wall thickness and length of honeycomb cell.[29)] The parameter $I$ is rotary inertia and $M$ is mass. The subscript $i$ refers to the index of each layer, and $n$ is the total number of layers, as shown in Fig. 2.6. The panel is symmetric with respect to the neutral plane, which is parallel to the $xy$-plane, and Fig. 2.6 shows $l_i$ defined as the distance between the neutral plane and the surface of each

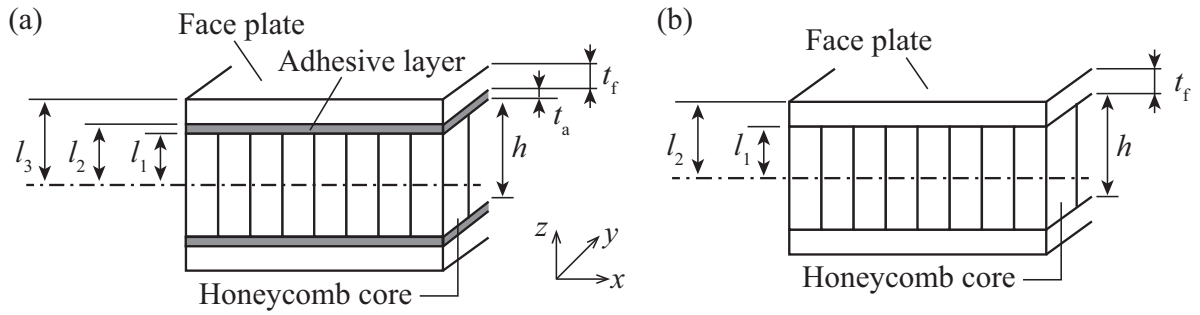


Figure 2.6: Structures of honeycomb sandwich panel: (a) five-layered model and (b) three-layered model.

layer. The density of each layer is expressed as $\rho_i$. In addition, the natural frequency of the fundamental thickness-shear mode $\omega_{\mathrm{TS}}$ was calculated using the transmission-line model.[30)]

**Calculation of natural frequency of the fundamental thickness-shear mode based on the transmission-line model** We derived the natural frequency of the fundamental thickness-shear mode $\omega_{\mathrm{TS}}$ from calculations based on the transmission-line model. Figure 2.7 shows the transmission-line model of a three-layered sandwich panel. The sandwich panel is modeled as a one-dimensional transmission line. The characteristic impedance and propagation velocity of the shear wave in each layer are differ when the thickness of each layer is assumed as the length $t$ of each transmission line. The impedance $Z_i$ of each layer is obtained using the following equations:

$$Z_i = R_i \frac{Z_{i-1} + jR_i \tan \gamma_i t_i}{R_i + jZ_{i-1} \tan \gamma_i t_i}, \tag{2.10}$$

$$R_i = \sqrt{\rho_i c_{55i}}, \tag{2.11}$$

$$\gamma_i = \omega \sqrt{\frac{\rho_i}{c_{55i}}}, \tag{2.12}$$

where $R$ and $\gamma$ are respectively the characteristic impedance and wavenumber of the shear wave obtained from the density $\rho$ and the stiffness modulus $c_{55}$ of each transmission line. Angular frequency is expressed as $\omega$. The natural frequency $\omega_{\mathrm{TS}}$ corresponds to the frequency at which the input impedance becomes zero.

**Elastic constants of honeycomb core** The calculation method the elastic constants $c_{11}$, $c_{13}$, $c_{33}$, and $c_{55}$ is indicated. When the honeycomb core layer is assumed as an orthotropic continuum, $c_{31}$ is equal to $c_{13}$. An ideal honeycomb cell is formed with a regular hexagon whose walls have identical thicknesses. In practice, two walls of the cell are double the thicknesses of the others because a honeycomb core is made by bonding cell walls together, as shown in Fig. 2.8. Young's modulus, shearing modulus of rigidity, and Poisson's ratio of the practical honeycomb core are calculated mathematically using the wall thickness and wall length of the cell. Table 2.2 shows the equivalent moduli proposed by Ogasawara et al., where $E_s$, $G_s$, and $\nu_s$ are the Young's modulus, modulus of rigidity, and Poisson's ratio of the material forming the cell, respectively. The core ratio $R$ is obtained using the wall thickness $a$ and the cell size $s$, $R = a/s$. The elastic

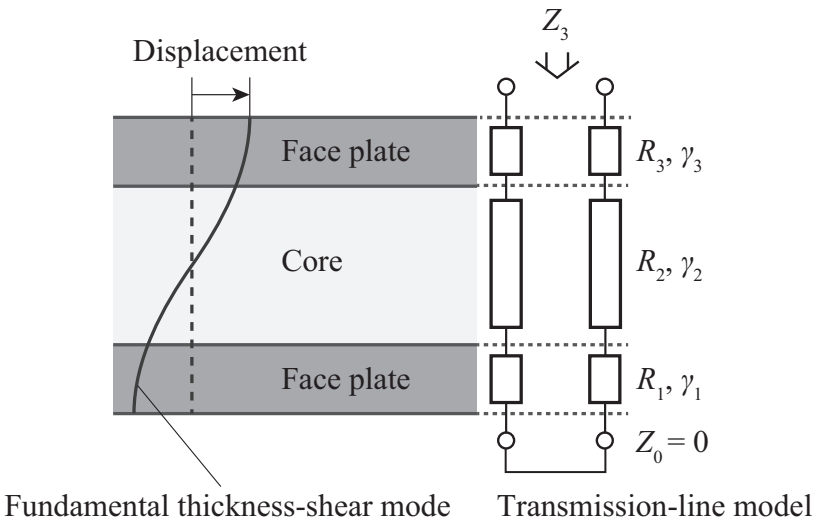


Figure 2.7: Transmission-line model of three-layered sandwich panel.

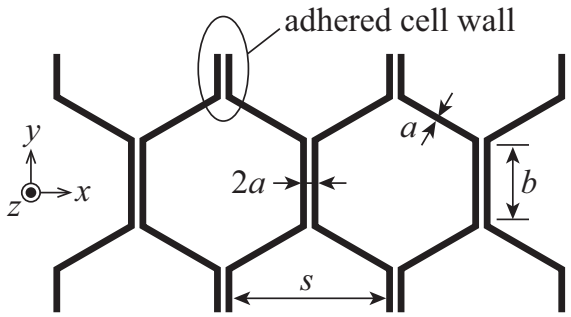


Figure 2.8: Cell form of practical honeycomb core in which two walls of a cell are double the thicknesses of the others because a honeycomb core is made by binding cell walls together.

constants of the honeycomb core layer were obtained from the parameters in Table 2.2 by assuming the core as an orthotropic continuum. Here, it was found that flexural stiffness was diverged when $\nu_{xy}$ was 1. Therefore, we calculated the elastic constants of the honeycomb core layer by approximating $\nu_{xy}$ by 0.999 since an alteration of $v_\mathrm{p}$ by the approximation of $\nu_{xy}$ was extremely small. In the five-layered sandwich panel, the elastic constants of the face panel and adhesive layer are determined on the basis of the physical parameters of each layer. On the other hand, we can treat the five-layered sandwich panel as a three-layered panel by assuming that the face panel is combined with the adhesive layer. In this work, we calculate the theoretical value of the phase velocity $v_\mathrm{p}$ of the flexural wave in a honeycomb sandwich panel by these mathematical methods.

**Calculation of phase velocity of flexural wave propagating on sandwich panel** Here, the general solutions of Eqs. (2.4) and (2.5) are assumed such that $w = A\exp\left[j(\omega t - k_\mathrm{p}x)\right]$ and $\psi = B\exp[j(\omega t - k_\mathrm{p}x)]$, where $k_\mathrm{p}$ is the wavenumber of the flexural wave. Amplitude is expressed as $A$ and $B$. By eliminating

Table 2.2: Equivalent material properties.

| Young's modulus | Modulus of rigidity | Poisson's ratio |
|---|---|---|
| $E_x = 12R^3E_s$ | $G_{xy} = \frac{36}{5}RG_s$ | $\nu_{xy} = 1$ |
| $E_y = 12R^3E_s$ | $G_{yz} = \frac{5}{3}RG_s$ | $\nu_{yz} = \frac{9}{2}R^2\nu_s$ |
| $E_z = \frac{8}{3}RE_s$ | $G_{xz} = RG_s$ | $\nu_{xz} = \nu_s$ |

Table 2.3: Physical parameters of honeycomb sandwich panel.

| Parameter | Value | Reference cited |
|---|---|---|
| Thickness of face plate $t_\mathrm{f}$ (mm) | 1 | 3A Composites, ALUCORE |
| Thickness of adhesive layer $t_\mathrm{a}$ (mm) | 0.12 | Thompson et al.[28] |
| Height of honeycomb core $h$ (mm) | 13 or 23 | 3A Composites, ALUCORE |
| Wall thickness of honeycomb core $a$ ($\nu$m) | 70 | 3A Composites, ALUCORE |
| Cell size of honeycomb core $s$ (mm) | 6.35 | 3A Composites, ALUCORE |
| Density of face plate $\rho_\mathrm{f}$ (kg/m$^3$) | 2660 | 3A Composites, ALUCORE |
| Density of adhesive layer $\rho_\mathrm{a}$ (kg/m$^3$) | 5292 | Thompson et al.[28] |
| Density of cell material $\rho_\mathrm{c}$ (kg/m$^3$) | 2730 | 3A Composites, ALUCORE |

$A$ and $B$ after substituting the general solutions into Eqs. (2.4) and (2.5), we obtain the following equation:

$$\{KM + (DM + KI)\,k^2\}\omega^2 - DKk^4 - IM\omega^4 = 0. \tag{2.13}$$

The wavenumber of the flexural wave $k_\mathrm{p}$ is expressed using the angular frequency $\omega$ and the phase velocity $v_\mathrm{p}$ of the flexural wave in the sandwich panel; $k_\mathrm{p} = \omega/v_\mathrm{p}$. The phase velocity $v_\mathrm{p}$ is obtained using the following equation:

$$v_\mathrm{p}^2 = \frac{\omega^2\,(DM + IK) - \omega\sqrt{\omega^2\,(DM + KI)^2 - 4MDK\,(\omega^2 I - K)}}{2M\,(\omega^2 I - K)}. \tag{2.14}$$

The theoretical value was calculated by substituting these parameters into Eq. (2.14). Table 2.3 shows the structural parameters of a honeycomb sandwich panel used for theoretical equations (3A Composites ALUCORE). In addition, Table 2.4 shows the elastic constants of face plate, honeycomb core, and adhesive layer of the honeycomb sandwich panel obtained using the parameters listed in Table 2.3. The adhesive layer was assumed as HT 42 type III. We used the parameters for the theoretical equations to calculate the theoretical $v_\mathrm{p}$ value of the three-layered panel in this study.

### 2.3.2 Simulation using finite element method

Next, two models of the sandwich panel was simulated. Figures 2.9 shows the finite element divisions and coordinates of these models. The honeycomb sandwich panel was modeled by shell elements using simulation software (COMSOL Multiphysics 4.4) based on FEM, as shown in Fig. 2.9(a). This model is called the honeycomb model in this paper. The form of the honeycomb cell was the same as that of the previous section, and the crossover of the cell wall was double the thicknesses of the others. In addition, we

Table 2.4: Elastic constants of honeycomb sandwich panel (GPa).

| Elastic constants of faceplate | |
|---|---|
| $c_{11}$ | 200 |
| $c_{13}$ | 49.72 |
| $c_{33}$ | 200 |
| $c_{55}$ | 25.56 |
| **Elastic constants of honeycomb core** | |
| $c_{11}$ | $3.1281 \times 10^{-3}$ |
| $c_{13}$ | $1.86 \times 10^{-3}$ |
| $c_{33}$ | 2.06 |
| $c_{55}$ | $2.90 \times 10^{-1}$ |
| **Elastic constants of adhesive layer** | |
| $c_{11}$ | 9.90 |
| $c_{13}$ | 4.24 |
| $c_{33}$ | 9.90 |
| $c_{55}$ | 2.83 |

simulated another model that has the orthotropic continuum core, which was given physical parameters by Tables 2.3 and 2.4. This model is called the simplified model in this paper, as shown in Fig. 2.9(b). In both simulations, the face plate including the adhesive layer was treated as a single shell, which was the given physical parameters of the three-layered panel. All the boundaries and edges of the plate were mechanically free. The length $L$ in the $x$-direction of the panels is 1,000 mm, and the width $W$ in the $y$-direction is 11 mm, as shown in Fig. 2.9(c). The natural frequencies $f_N$ of the flexural wave in the $x$-direction were simulated, and the frequency dependence of the phase velocity $v_\mathrm{p}$ was given by the general expression $v_\mathrm{p} = 2Lf_N/N$, where $N$ is the number of half wavelengths in the panels.

### 2.3.3 Measurement of phase velocity

Finally, the phase velocity of the flexural wave in the sandwich panel was measured experimentally. Figure 2.10 shows the experimental arrangement for impulse response measurement of the honeycomb sandwich panel. The wall length, thickness, and height of the honeycomb core were identical to those in the simulation. In the case of the core heights $h$ = 13 and 23 mm, the lengths $L$ in the $x$-direction of the panels are 1,956 and 2,186 mm, and the widths $W$ in the $y$-direction are 284 and 285 mm. The center and surface of the panel were defined as the origin of the $x$-coordinate, as shown in Fig. 2.10. The panel was suspended by two light strings in order to assume that the panel was mechanically free. A microphone array consisting of 7 microphones whose interval was 40 mm was scanned from -1,000$\leq x \leq$1,000 mm every 50 mm to calculate the signal received at each point. The microphones were maintained under 5 mm distance from the surface of the panel. The time-stretched pulse (TSP) signal was used as the driving signal, and the impulse response of the panel at each receiving point was obtained after pulse compression. The number of samples of the TSP signal was 65,536, and the amplitude of the TSP signal applied to an electromagnetic

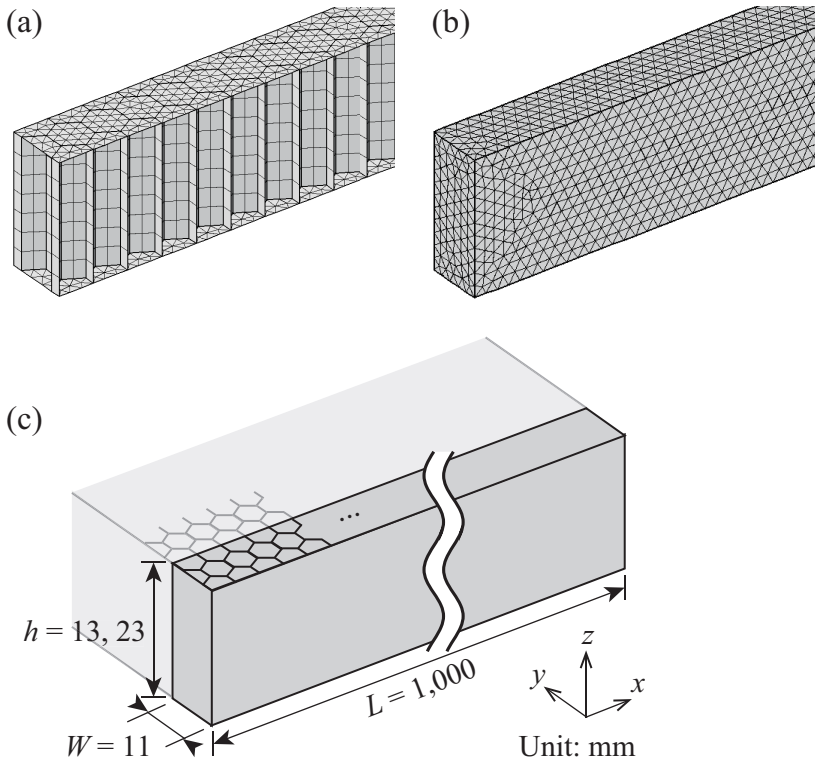


Figure 2.9: Outline of the honeycomb sandwich panels in FEM simulation: (a) finite element division with shell elements, (b) finite element division with solid element, and (c) coordinates and size of the panel.

exciter (Brüel & Kjær 4809) was 6 V. The signals received by the microphones were sampled at 50 kHz by an analog-to-digital converter (NI USB-6212). The dispersion curve of $v_{\mathrm{p}}$ with respect to each spatial frequency was calculated by the method using the wavenumber spectrum indicated in the previous section. Modal distribution exists in the $y$-direction as well as in the $x$-direction because the width $W$ is not sufficiently small with respect to the length $L$ of the panel used in the experiment. In this study, we indicate the phase velocity $v_{\mathrm{p}}$ in the case of the 0th-order mode in the $y$-direction by averaging the impulse response of the microphone array so that the panels can be assumed as beams.

### 2.3.4 Results and discussion

Figure 2.11 shows the frequency characteristics of the phase velocity of the flexural wave in the panels. The results in the case of $h$ = 13 and 23 mm are shown in Figs. 2.11(a) and 2.11(b), respectively. Curve a with a solid line indicates the theoretical $v_{\mathrm{p}}$ value calculated using Eq. (2.14). The circle and cross marks also show $v_{\mathrm{p}}$ in FEM simulation in the honeycomb model and simplified model, respectively. Here, in order to find the difference between the honeycomb sandwich panel and the homogeneous plate in the dispersion of $v_{\mathrm{p}}$, the $v_{\mathrm{p}}$ values of homogeneous plates were also calculated using Eq. (2.3). Curves b and c indicate the $v_{\mathrm{p}}$ values of the homogeneous plates A and B, respectively. The thicknesses of the homogeneous plates A and B were set as 20 and 1 mm, respectively. $v_{\mathrm{p}}$ of the homogeneous plate A was higher than the sound velocity in air at a frequency identical to that of the honeycomb sandwich panel ($h$ = 13 mm). The material

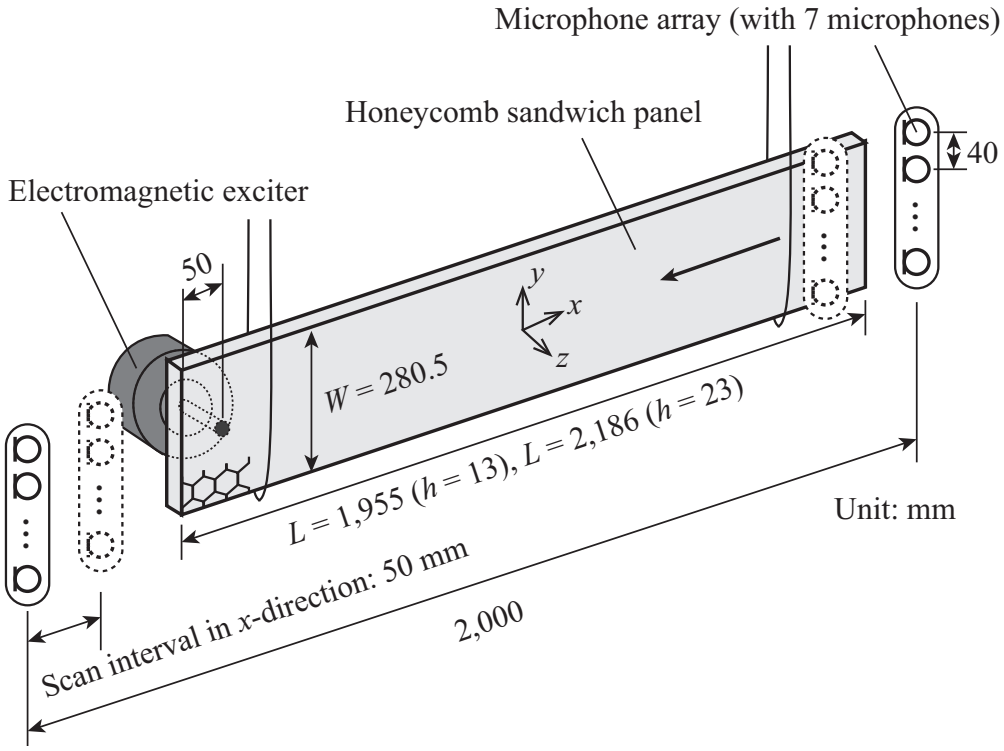


Figure 2.10: Experimental arrangement for impulse response measurement of honeycomb sandwich panel.

properties of the homogeneous plates A and B were the same as those of the face plate. Curve b shows the sound velocity in air (340 m/s). The experimental value of $v_{\mathrm{p}}$ is shown by the darker-shaded area. The power was normalized by the maximum power of each frequency.

We focused on the frequency dispersion of the phase velocity $v_{\mathrm{p}}$. The curve that appeared in the frequency band of $1 \leq f \leq 2.5$ kHz, as shown in Fig. 2.11(a), is $v_{\mathrm{p}}$ in the case of the 2nd-order mode in the $y$-direction. This curve was ignored in this study in order to assume that the panels are beams since we focused on $v_{\mathrm{p}}$ in the case of the 0th-order mode in the $y$-direction. The results of the honeycomb model shown as circles and the simplified model shown as cross marks were in good agreement with that obtained using the theoretical equation. Here, it can be seen that the elastic constants of the honeycomb core layer obtained using the parameters of the cell form were properly estimated. In addition, it is possible to calculate $v_{\mathrm{p}}$ easily using theoretical equations that assumed the honeycomb core layer as an orthotropic continuum without the need to simulate the complex structure. Therefore, we compared between theoretical and experimental results. The dispersion of $v_{\mathrm{p}}$ in the experimental results shown as contrasting density became small in over $f$ = 3 kHz, and $v_{\mathrm{p}}$ approached asymptotically to around 600 m/s, as shown in Fig. 2.11. On the other hand, $v_{\mathrm{p}}$ in the theoretical results approached asymptotically to approximately 700 m/s. The theoretical results were in good agreement with the experimental values in the frequency band of $0 \leq f \leq 1$ kHz. However, a gap of asymptotic phase velocities was derived from the difference in the frequency at which the dispersion became small. It was confirmed that the frequency at which the dispersion became small depends on the natural frequency of the thickness-shear mode, $\omega_{\mathrm{TS}}$, which is determined by the modulus of rigidity and the density of the face plate. Therefore, $v_{\mathrm{p}}$ seems to be affected by the stiffness and mass of the adhesive

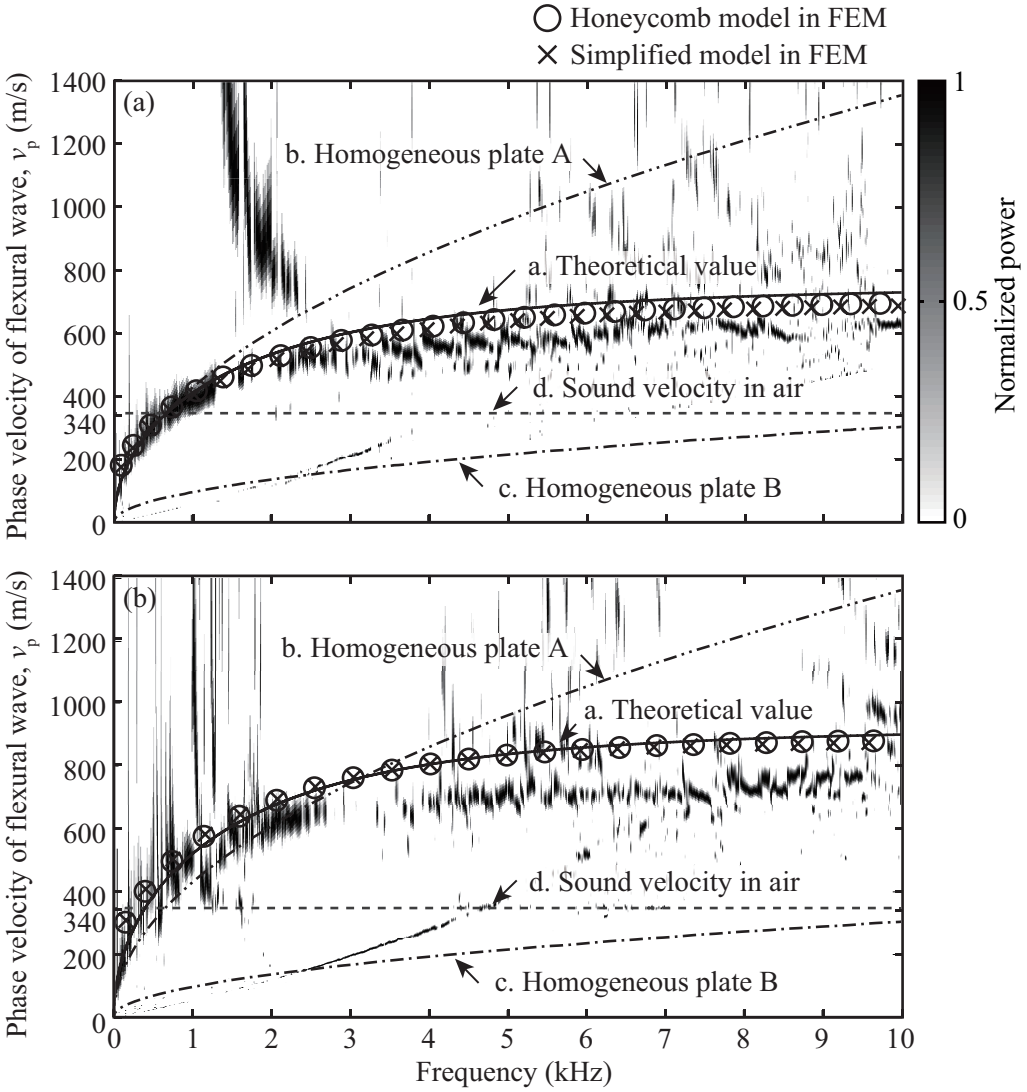


Figure 2.11: Frequency characteristics of phase velocity of the flexural wave in honeycomb sandwich panel and homogeneous plate: (a) $h$ = 13 mm and (b) $h$ = 23 mm.

layer summed into that of the face plate. The physical parameters of the adhesive layer were given not by the measured value but by the assumed value. According to this fact, the gap was presumably caused by the mass of the adhesive layer. However, it was clarified that the characteristics of the honeycomb sandwich panel can be predicted using the theoretical value and the simplified model.

## 2.4 Summary

The frequency characteristics of the phase velocity of the flexural wave propagating on a homogeneous panel and a honeycomb sandwich panel are analyzed. In the case of the homogeneous panel, the phase velocity that obtained using the motion equation of the beam was determined as the theoretical value. A planar transducer that consists of acrylic plastic plate was designed to measure the phase velocity of the

flexural wave. It was confirmed that the experimental value was in good agreement with the theoretical value.

In the case of the honeycomb sandwich panel, the calculation method of the phase velocity of the flexural wave was proposed. The theoretical value of the phase velocity was obtained using a plate equation by combining the full equation of motion of for elastic material and constitutive relations. The elastic constants of a honeycomb core layer was calculated using the shape and the physical property of the honeycomb cell to substitute into the theoretical equation. The honeycomb core layer was modeled by shell elements called the honeycomb model, and by the orthotropic continuum called the simplified model in the simulation using FEM. In addition, the phase velocity of the flexural wave was measured using the honeycomb sandwich panel made of aluminum to compare among the theoretical value, the simulated value, and the experimental value. The simulated value was well-accorded with the theoretical value. On the other hand, the gap between the theoretical value and the experimental value was caused due to the effect of the mass of the adhesive layer. However, it was indicated that the behavior of the honeycomb sandwich panel that was complex in structure can be predicted easily using the proposed method.

Using these knowledge, the acoustic transducer that generates the inclined plane wave and the evanescent sound field is designed by the calculation of the characteristics of the flexural wave.

# Chapter 3

# Application of inclined plane wave to flat panel loudspeaker

## 3.1 Background of flat panel loudspeaker

Audio guidance systems in public spaces have recently been receiving broad attention as not only barrier-free facilities but also information service making up for visual information.[31] In particular, evacuation guidance in the case of emergency requires a way for people to perceive the destination direction intuitively. The requirement of acoustic signal to localize sound image has been well investigated,[32] and an additional study for guidance sound has been reported.[33] On the other hand, there have been attempts to realize an escape guiding system that makes it easy to notice the destination direction by a unique sound generation technique using the precedence effect of audio signals.[34] The precedence effect uses an aural characteristic that a sound image is localized in the direction of the first coming sound when a number of the same sounds are generated with little time lag.[35] However, the method has a limitation such as varying the localized direction by reducing the effectiveness of the precedence effect near the loudspeaker since the difference in loudness between the subsequent sound and the first coming sound becomes small. Therefore, it is necessary for the guiding system to indicate the right direction regardless of position on a pathway.

To lead pedestrians using sound more accurately, we attempt to propose a loudspeaker for generating guiding sound, as shown in Fig. 3.1. We focused on sound radiation with an inclined angle from a flexural wave propagating in an elastic panel, and it was considered as inclined plane wave. The mechanism is the same as that of the leaky Lamb wave. In the past, there had been no applications using the leaky Lamb wave for sound generation in auditory frequency. Therefore, we first attempted to find the requirement for inclined plane wave generation in auditory frequency. The inclined plane wave is radiated in air when the phase velocity of the flexural wave is larger than the sound velocity in air. It was confirmed that a vibration plate requires high stiffness and low density, similarly to beryllium, in order to generate a flexural wave with high phase velocity. In addition, in the case of a homogeneous elastic plate, the phase velocity of the flexural wave has dispersion, which causes dispersive group delay and radiation angle variance with increasing frequency. Therefore, a homogeneous plate is unsuitable for generating guiding voice and the proposed loudspeaker is still a challenge. On the other hand, a sandwich plate that consists of two face

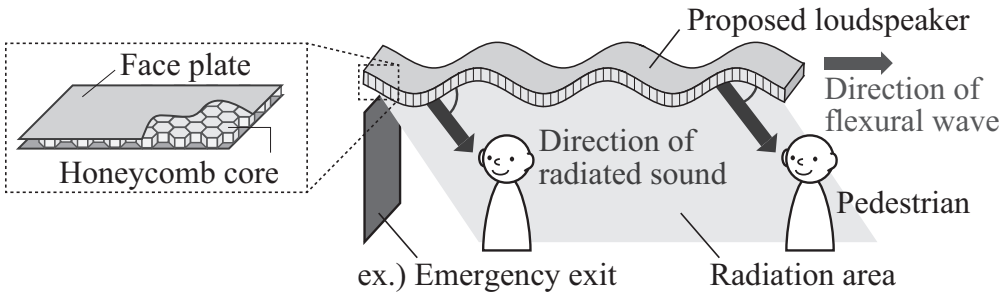


Figure 3.1: Proposed loudspeaker for audio guidance system using honeycomb sandwich panel.

plates and an interjacent honeycomb core layer is a well-known material given its hardness and lightness. Furthermore, a study has shown that the dispersion of the phase velocity becomes smaller with increasing frequency in the auditory frequency band. The characteristics are attractive for generating voice-guiding navigation; hence, in this study, we aim to construct a sound radiator using a honeycomb sandwich panel.

## 3.2 Principle of generation of sound by flexural wave

In two-dimensional problem, the physical quantity in the acoustic field adjacent to a plate is homogeneous in the $y$ direction. Velocity potential $\phi$ is written in the wave equation

$$\frac{1}{c^2}\frac{\partial^2\phi}{\partial t^2} = \frac{\partial^2\phi}{\partial x^2} + \frac{\partial^2\phi}{\partial z^2}. \tag{3.1}$$

The general solution of the wave equation is expressed as

$$\phi(x,z) = A\exp\left[-j(k_x x + k_z z)\right]\exp\left(j\omega t\right), \tag{3.2}$$

where $c$ is sound velocity in the air, $k_x$ and $k_z$ are components in the $x$ and $z$ directions of the wave number vector $\boldsymbol{k}$. Particle velocity of the air requires to be coincident with normal velocity of the plate $u$ on the boundary ($z = 0$) in Eq. (2.2);

$$\frac{\partial\phi}{\partial z} = -j\omega u. \tag{3.3}$$

$x$ component of wavenumber in the acoustic field $k_x$ equals the plate wavenumber $k_\mathrm{p}$. In addition, the sound pressure is expressed using the velocity potential.

$$p(x,z) = \rho\frac{\partial\phi}{\partial t}, \tag{3.4}$$

where $\rho$ is the density of air. Then, the general equation of the sound pressure is obtained as following equation:

$$p(x,z) = j\omega\rho A\exp\left[-j(k_x x + k_z z)\right]\exp\left(j\omega t\right). \tag{3.5}$$

When the phase velocity of the flexural wave, $v_\mathrm{p}$, is greater than the sound velocity in the air, $c$: $k_\mathrm{p}<|\boldsymbol{k}|$, inclined plane wave radiate from the surface of the plate as shown in Fig. 3.2(a). The theoretical radiation

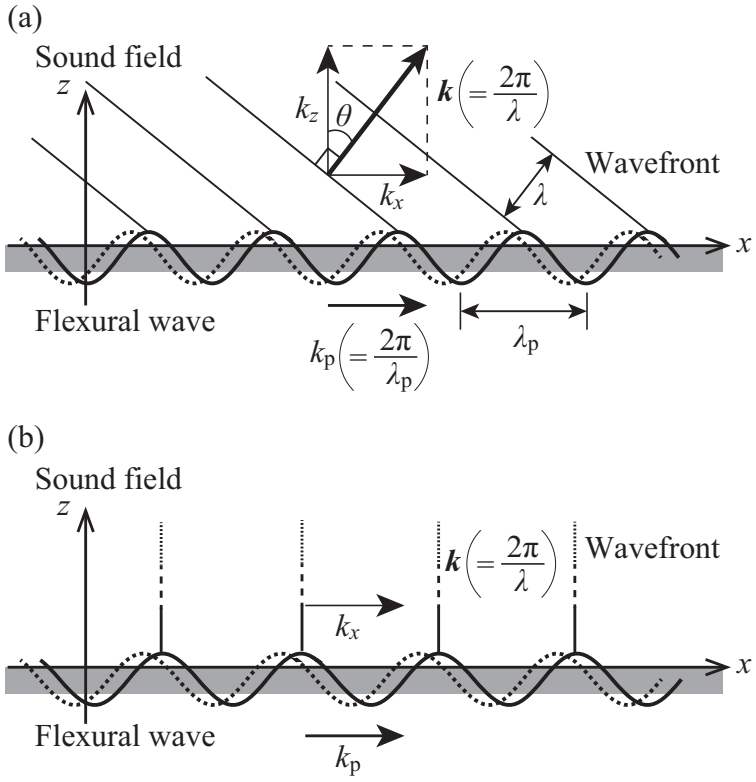


Figure 3.2: Sound generation from flexural wave propagating on a plate: (a) Phase velocity of flexural wave is greater than the sound velocity in the air: $k_\mathrm{p}<|\boldsymbol{k}|$ and (b) phase velocity is smaller than the sound velocity: $k_\mathrm{p}>|\boldsymbol{k}|$.

angle $\theta$ with respect to the $z$-axis is obtained using $v_\mathrm{p}$ and the sound velocity in air, $c$, as using the following equation:[36)]

$$\tan\theta = \sqrt{|\boldsymbol{k}|^2/k_\mathrm{p}^2}. \tag{3.6}$$

On the other hand, $k_\mathrm{z}$ is pure imaginary number when phase velocity is smaller than the sound velocity: $k_\mathrm{p}>|\boldsymbol{k}|$ as shown in Fig. 3.2(b). Thereby, it is found that the sound pressure $p$ attenuates exponentially with the distance from the plate in the $z$-direction. In this situation, the sound is not radiated to far field but the evanescent sound field is generated in the region adjacent to the plate surface.

## 3.3 Design of flat panel loudspeaker using inclined plane wave

### 3.3.1 Design procedure of loudspeaker generating inclined plane wave

For the realization of the proposed loudspeaker for the audio guidance system, the loudspeaker has to be designed to satisfy the following requirements.

- $v_\mathrm{p}$ is larger than the sound velocity in air in auditory frequency.
- The group delay dispersion is small in auditory frequency.

- The loudspeaker can be driven by a realistic actuator.

We found that the theoretical value and the simplified model are applicable to the prediction of the characteristics of the honeycomb sandwich panel, as mentioned in the previous sections. Therefore, the design procedure using the theoretical equation and the simplified model is given below:

(1) Shape and physical properties of the face plate, the adhesive layer, and the honeycomb core are assumed.

(2) $\omega_{\mathrm{TS}}$ is calculated using the parameters of (1).

(3) $D$, $K$, $I$, and $M$ are calculated by substituting the parameters of (1) and (2) into Eqs. (2.6) – (2.9).

(4) The frequency characteristics of $v_{\mathrm{p}}$ and $v_{\mathrm{g}}$ are obtained using the parameters of (3).

(5) Steps (2) – (4) are repeated while changing the parameters so as to obtain the desired dispersion.

We performed steps (1) – (4) in the previous sections. Now, we attempt to design the optimized loudspeaker after verifying how the parameters of the panel affect $v_{\mathrm{p}}$ and $v_{\mathrm{g}}$. Figure 3.3(a) shows the frequency characteristics of $v_{\mathrm{p}}$ and $v_{\mathrm{g}}$ with varying the core height $h$ when the cell size $s$ is 6.35 mm. The solid line and dotted line indicate $v_{\mathrm{p}}$ and $v_{\mathrm{g}}$, respectively. It is found that $v_{\mathrm{p}}$ increased rapidly at low frequency with increasing $h$. As a result, $v_{\mathrm{p}}$ and $v_{\mathrm{g}}$, which become constant with respect to frequency, become large. Figure 3.3(b) shows the frequency characteristics of $v_{\mathrm{p}}$ and $v_{\mathrm{g}}$ with varying the cell size $s$ when the core height $h$ is 23 mm. The solid line and dotted line also indicate $v_{\mathrm{p}}$ and $v_{\mathrm{g}}$, respectively. It appears that the frequency, at which the dispersion of $v_{\mathrm{p}}$ becomes constant, becomes lower with increasing $s$. The modulus of elasticity of the core depends on the cell size $s$. However, $v_{\mathrm{g}}$ increased excessively at low-frequency band when $s$ was large. Consequently, the group delay dispersion became large at low frequency. Therefore, we have to choose optimum parameters. The bold-solid line and bold-dotted line in Fig. 3.3(b) indicate $v_{\mathrm{p}}$ and $v_{\mathrm{g}}$ of the honeycomb sandwich panel whose $h$ is 23 mm and $s$ is 25.4 mm, respectively. The other parameters were identical to those of the honeycomb sandwich panel described in the previous sections. In the case of this panel, it is found that $v_{\mathrm{p}}$ was larger than 340 m/s when $f \geq$300 Hz. In addition, $v_{\mathrm{g}}$ had a small dispersion when $f \geq$1 kHz. Therefore, this panel is called the optimized model. Additionally, we simulate sound radiation by the proposed loudspeaker to confirm its realizability.

### 3.3.2 Simulation of generating inclined plane wave using finite element method

Figure 3.4 shows the shape of the proposed loudspeaker with sound field and boundary conditions in the simulation. In order to find the difference between the honeycomb sandwich panel and the homogeneous plate in terms of mobility, the homogeneous plate A in the previous section was also simulated. Since these models were symmetric with respect to the $xz$-plane, only one side of the model across the symmetry plane was simulated so as to reduce computational effort. The length was $L$ = 2,000 mm, and the width was $W/2$ = 5.5 mm. In the cases of the optimized model and the homogeneous plate, the core heights were defined as $h$ = 23 and 20 mm, respectively. Rayleigh damping is introduced for convenience instead of the damping material for attenuating vibration. The stiffness damping coefficient $\beta$ was introduced in order to

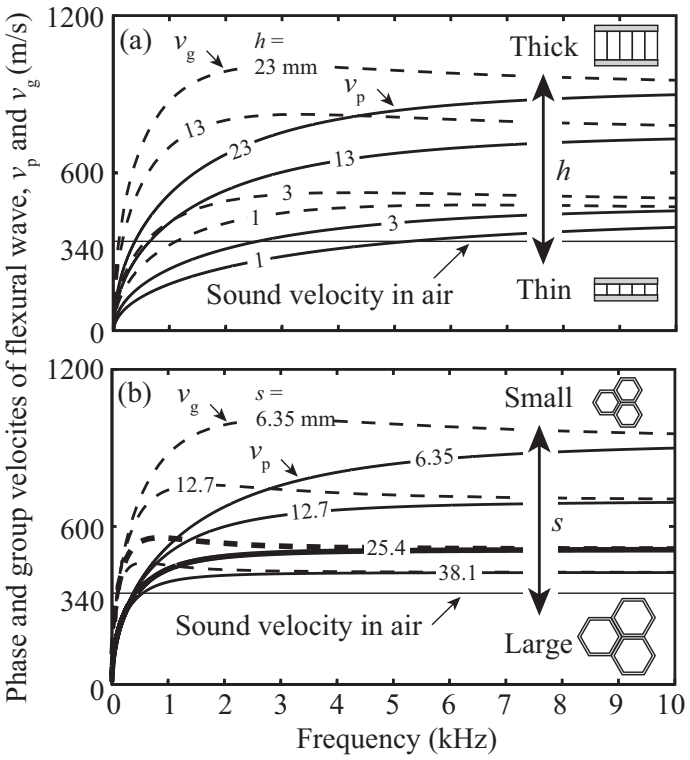


Figure 3.3: Frequency characteristics of phase and group velocities of the flexural wave: (a) with varying only the core height $h$ when the cell size $s$ is 6.35 mm, and (b) with varying only the cell size $s$ when the core height $h$ is 23 mm.

generate only traveling wave, as shown in Fig. 3.4(b). The minimum value of $\beta$ was 0 at $x$ = 200 mm, and $\beta$ increased linearly with respect to the $x$-coordinate. The maximum values of $\beta$ at $x$ = 1,000 mm were 0.8. The boundary of the sound field was the absorbing boundary condition. The rigid wall was placed at the same height as the surface of the plate, as shown in Fig. 3.4(a). The frequency response of the flexural wave on a plate and the generated sound field were simulated in three-dimensional space using a finite element simulation software (COMSOL Multiphysics 4.4). The computational domain was divided by the tetrahedral element whose maximum edge size was 54 mm. The number of elements was 232,236, and the degrees of freedom were 331,704. A force load of 3.025 $\times 10^{-4}$ N was applied at a driving area assumed as an electromagnetic exciter. The elastic wave field was coupled with the sound field through the interface. The interface interchanges the particle velocity of the elastic wave in the normal direction and the particle velocity of the sound field. In addition, the pressure of the sound field was input into the surface of the loudspeaker.

### 3.3.3 Results and discussion

Figure 3.5 shows the distribution of the sound intensity generated by the proposed loudspeakers. Figures 3.5(a) – 3.5(c) and 3.5(d) – 3.5(f) indicate the results of the optimized model and the homogeneous plate A, respectively. The length of arrows was indicated as a logarithmic expression whose maximum

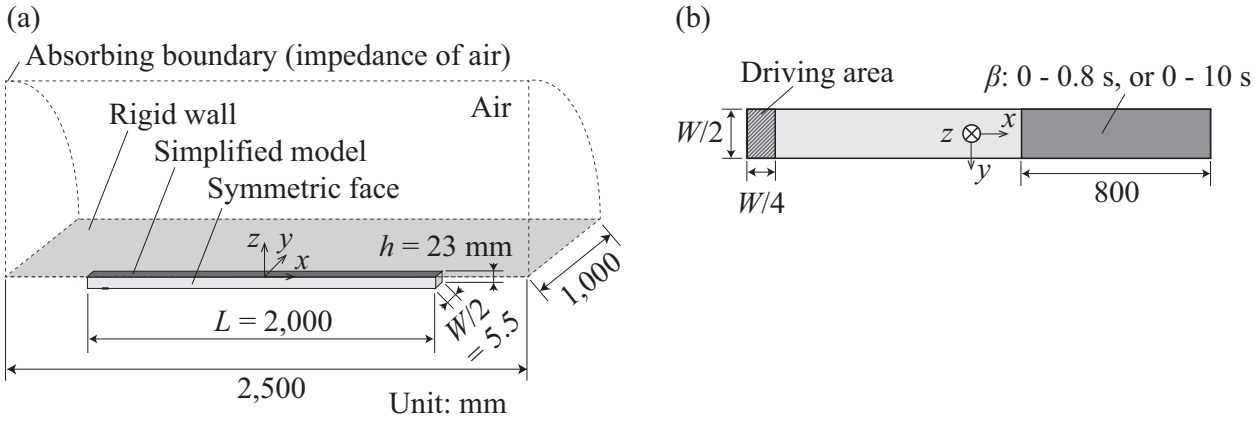


Figure 3.4: Outline of FEM simulation: (a) shape of the proposed loudspeaker and boundary conditions and (b) size of the panel.

vector length of sound intensity in each sound field was defined as $10^3$. It can be seen that inclined plane wave radiated from the loudspeaker at each frequency which meets the condition of sound radiation. Here, we focused on the radiation angle. $v_{\mathrm{p}}$ values of the optimized model and the homogeneous plate A were obtained and shown in Figs. 3.3 and 2.11, respectively. The simulated radiation angle was calculated using an average of the sound intensity in the line whose $x$- and $z$-coordinates were from (-0.5, 0.5) to (0.5, 0.5). Figure 3.6 shows the frequency characteristics of the theoretical and simulated radiation angles. The solid line and circle mark show respectively the theoretical and the simulated value of the optimized model. The dotted line and cross mark also show the theoretical and the simulated value of the homogeneous plate A. In the case of the optimized model, the difference between the theoretical and the simulated value was from 0.015 to 0.063 rad. On the other hand, in the case of the homogeneous plate, the difference between the theoretical and the simulated value was from 0.005 to 0.071 rad. It was confirmed that the radiation angle can be roughly predicted using the theoretical $v_{\mathrm{p}}$ value. The prediction of the sound field is required for the design of the proposed loudspeaker. In addition, the variance of the radiation angle with the change in the frequency of the optimized model was small. This characteristic of radiating sound with uniform angle is useful for indicating the direction of the destination. Therefore, the proposed loudspeaker using the honeycomb sandwich panel is suitable for audio guidance systems.

## 3.4 Summary

A flat panel loudspeaker using inclined plane wave for generating guiding sound was proposed. The inclined plane wave is radiated in air when the phase velocity of the flexural wave is larger than the sound velocity in air. The honeycomb sandwich panel was designed for generating inclined plane wave by changing the core height and the cell size. It was found that the phase velocity and the group velocity of the flexural wave increased rapidly at low frequency with increasing the core height. In addition, the phase velocity dispersion becomes constant at low frequency with increasing the cell size. The sound radiation from the designed panel was simulated using FEM. It was confirmed that the characteristic of radiating sound with

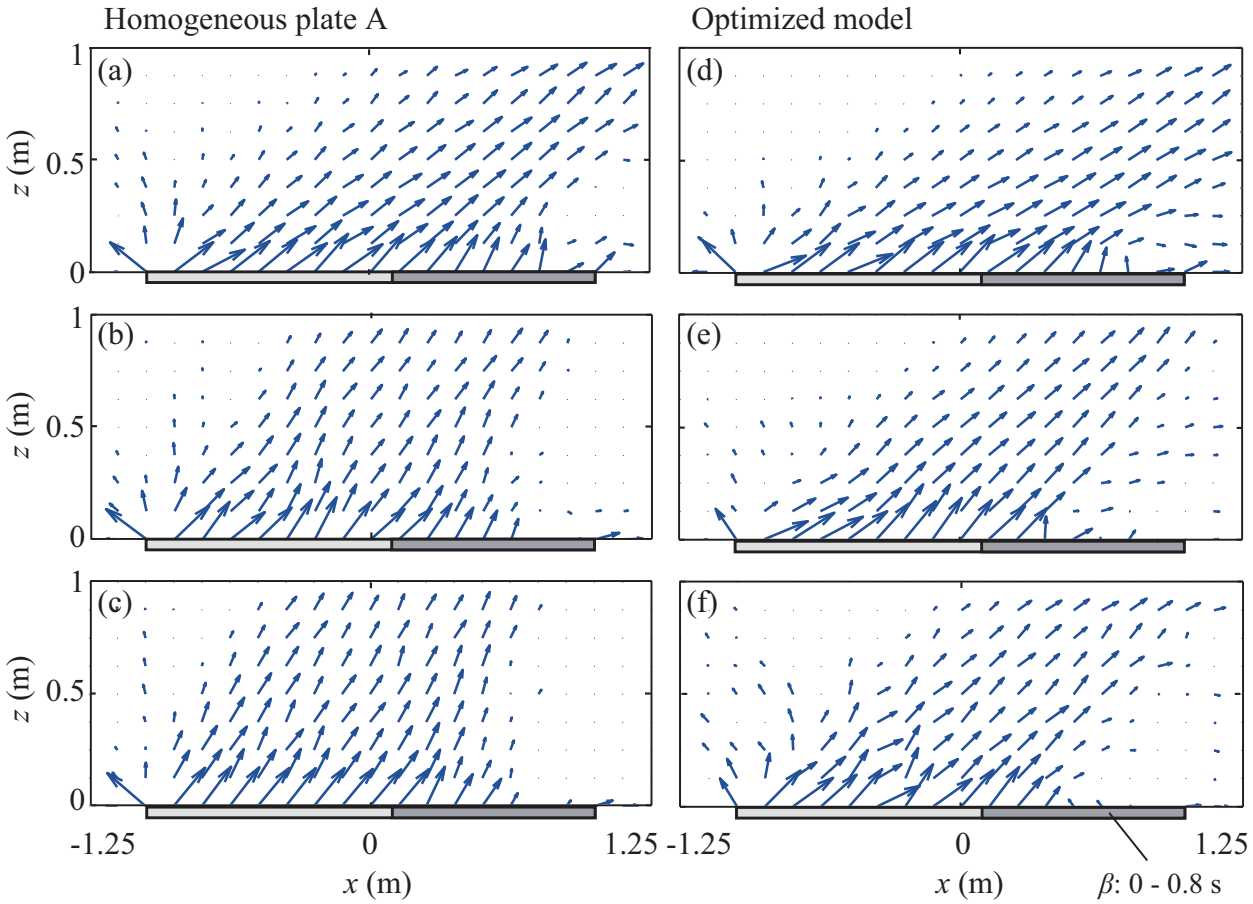


Figure 3.5: Distribution of sound intensity of the sound field on the $xz$-plane in the simulation: (a) driving frequency $f$ = 1 kHz, (b) $f$ = 2 kHz, and (c) $f$ = 3 kHz in the case of the homogeneous plate A. (d) driving frequency $f$ = 1 kHz, (e) $f$ = 2 kHz, and (f) $f$ = 3 kHz in the case of the optimized model.

uniform angle is useful for indicating the direction of the destination. The obtained results suggested that the proposed loudspeaker using a honeycomb sandwich panel is suitable for audio guidance systems.

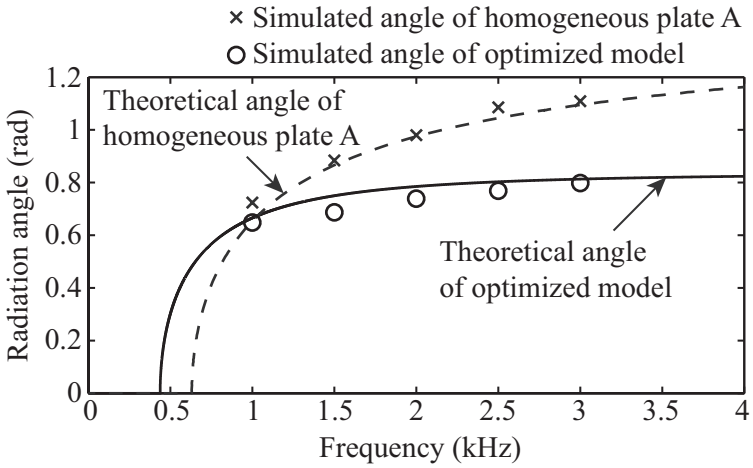


Figure 3.6: Frequency characteristics of theoretical and simulated radiation angles in the cases of the optimized model and the homogeneous plate A.

# Chapter 4

# Application of evanescent sound field to near-field acoustic communication system

## 4.1 Background of near-field acoustic communication system

Along with the popularization of mobile devices, various communication methods have actively been used; e.g., IC cards using electromagnetic wave, optical data communication using infrared ray. These methods are utilized for one-on-one communication with high-security level such as electronic payment because the area where data signal can be reached by a mobile device is limited.[37–39] However, these methods require extra hardware, which is essentially needless for mobile devices. Such a hardware prevents reduction in size and weight of devices. Therefore, acoustic data communication method for mobile devices has recently received broad attention. The acoustic data communication is attractive because the method requires only loudspeaker and microphone those are originally attached to mobile devices.[40,41] Acoustic data communication has been used mainly in underwater acoustic communication because acoustic wave in underwater can propagate longer distance than electromagnetic wave.[42,43] On the other hand, acoustic data communication for short-range in air has not been well researched except for use of indoor positioning (acoustic beacon).[44,45] However, near-field acoustic communication method has not well been researched nor used. If near-field acoustic communication method is realized, this method would limit the area reaching acoustic data signal to a mobile device, and be utilized for one-on-one communication such as IC cards as shown in Fig. 4.1. Furthermore, localized sound generation keeps silent environment because the sound does not propagate in the distance. Therefore, we propose suitable device for near-field acoustic communication for mobile devices.

In this study, evanescent sound field is utilized for generating sound in near-field. We focused on that evanescent sound field decays along a distance between sound source and receiving point. This study aims to construct a planar acoustic transducer generating the evanescent sound field. The fabrication of the planar acoustic transducer is simpler than the array shape. In addition, from viewpoint of application utilized for acoustic communication with mobile devices, we need to generate the evanescent sound field in audio

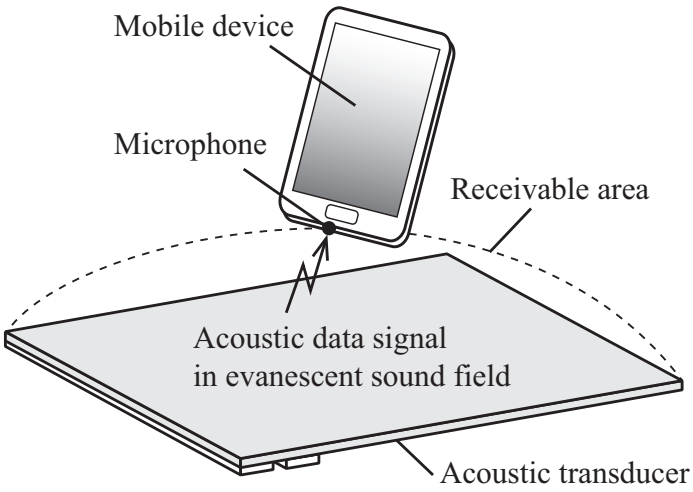


Figure 4.1: Near-field acoustic communication system using an evanescent sound field generated near the surface of a vibration plate.

frequency with large level enough to receive by mobile devices equipped with microphones. In this paper, we design the acoustic transducer for generating the evanescent sound field by the theoretical equation to meet these conditions. Moreover, the acoustic transducer is made with design-based shape, and the distribution of sound pressure level of the acoustical field above the acoustic transducer is measured in the simulation and experiment. Finally, the applicability of the realization of near-field acoustic communication system using the proposed acoustic transducer is indicated.

## 4.2 Generation of evanescent sound field by planar acoustic transducer

### 4.2.1 Simulation of generating evanescent sound field using finite element method

Figure 4.2 shows the shape of a planar acoustic transducer and boundary conditions in the simulation. Since these models were symmetric with respect to the $xz$-plane, only one side of the model across the symmetry plane was simulated so as to reduce computational effort. The conditions of the panel and the piezoelectric ceramic transducer were identical with those in the simulation. The boundary of sound field was absorbing boundary condition, and the boundary which was placed at same height with surface of plate was rigid wall. A frequency response of the flexural wave on a plate and generated sound field were simulated in three dimensional space using a finite element simulation software (COMSOL Multiphysics 4.2). Input voltage to piezoelectric transducer was assumed to 10 V. Elastic wave field was coupled with sound field through the interface. The interface interchanges particle velocity of elastic wave in normal direction and particle velocity of sound field.

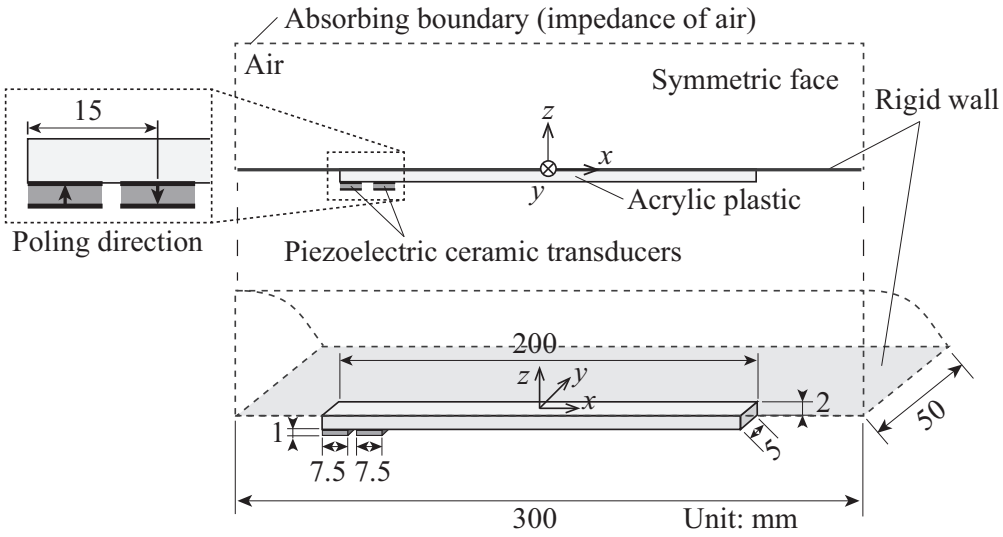


Figure 4.2: Shape of a planar acoustic transducer and boundary conditions in the simulation.

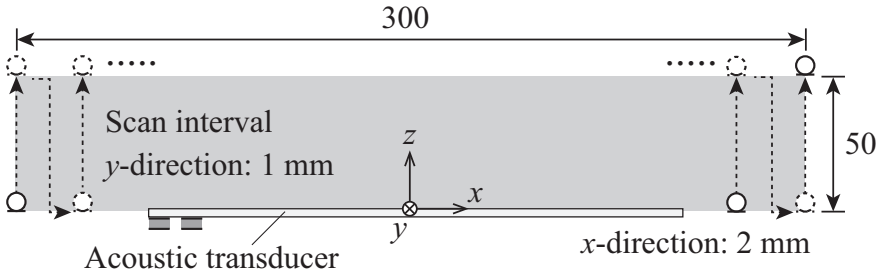


Figure 4.3: Scan area of a probe microphone in sound field on a planar acoustic transducer, and scan interval of $xz$-axes.

### 4.2.2 Experiment of generating evanescent sound field

Figure 4.3 shows the scan area of a probe microphone in sound field on a planar acoustic transducer, and scan interval of the $xz$-axes. The conditions of the plate and the piezoelectric ceramic transducer were identical with those in the simulation. We used a probe microphone that was identical to the microphone in the previous section. The probe microphone was scanned to calculate received signal at each point. The center and the surface of plate was defined as the origin of the $xz$-coordinates as shown in Fig. 4.3. The probe microphone was scanned between -150≤$x$≤150 mm for every 1 mm, and 0≤$z$≤50 mm for every 2 mm. Time stretched pulse (TSP) signal was used as driving signal, and the impulse response of the acoustic transducer at each receive point was obtained. The number of sampling of TSP signal was 65,536, and the amplitude of TSP signal was 10 V. Received signal by the probe microphone was sampled at 100 kHz by Analog-Digital converter (NI USB-6212).

### 4.2.3 Results and discussion

The sound field of a piston sound source was also simulated in order to compare attenuation distance of sound wave from the piston sound source with that of evanescent sound field. Normal particle velocity in the uniform amplitude and phase was input into the boundary corresponding to the surface of the proposed acoustic transducer. Only this case is pure acoustical analysis, in which the acoustic transducer is not included.

Figures 4.4 shows the sound pressure level of the sound field on the $xz$-plane in the simulation and the experiment. Figure 4.4(a) shows the result of piston sound source, $f$ = 10 kHz. Figures 4.4(b), 4.4(e) and 4.4(c), 4.4(f) show the results when driving frequency are 10 and 20 kHz, respectively. Figures 4.4(d) and 4.4(g) show the result when $f$ = 10 kHz with damped plate. Although vibration is attenuated by damping material actually, Rayleigh damping was introduced for convenience, and stiffness damping coefficient $\beta$ is introduced. When input voltage was 10 V, maximum sound pressure level were 85, 80, and 70 dB in case of 10 and 20 kHz, and 10 kHz with damping, respectively. These results are enough to be received by microphones of mobile devices.Attenuation of sound pressure level was compared. The distribution of sound pressure level in the experiment was mostly agrees with that in the simulation. Sound wave from the piston sound source propagated in the distance in Fig. 4.4(a). In contrast, the sound from the proposed acoustic transducer was highly attenuated under conditions generating the evanescent sound field as shown in Figs. 4.4(b), 4.4(d), 4.4(e), and 4.4(g). When driving frequency was 20 kHz, propagating wave was caused as shown in Figs. 4.4(c) and 4.4(f). In addition, according to Figs. 4.4(b), 4.4(c), 4.4(e), and 4.4(f), standing wave was caused by reflecting flexural wave at edge of the plate. If an evanescent sound field has nodes, a sound receiving area may be limited. However, in the case of the damped plate, an evanescent sound field was generated without nodes as shown in Figs. 4.4(c) and 4.4(g). Next, sound pressure level at $x$ = -25 mm is shown in Fig. 4.6. Curves a, b, c, and d correspond to sound pressure level when $f$ = 10, 20, and 10 kHz in the case of damped plate and $f$ = 10 kHz in the case of piston sound source, respectively. From the curves b and d in Fig. 4.6, sound pressure level was attenuated 20 dB at $z$ = 15 mm. On the other hand, sound pressure level was attenuated 20 dB at $z$ = 45 mm from the curves a and c in Fig. 4.6. It was confirmed that the proposed acoustic transducer can generate the evanescent sound field when phase velocity of the flexural wave is smaller than sound velocity in air ($f$ = 10 kHz and $f$ = 10 kHz with damped plate). According to these results, it was found that we can design the acoustic transducer generating the evanescent sound field in the simulation.

Finally, resonant frequency of the plate was compared. Figures 4.5 shows frequency characteristics of sound pressure level at ($x$, $z$) = (-25, 0) in the simulation and the experiment. Figure 4.5(a) shows the results of the plate without the damper, and Fig. 4.5(b) shows the results of the damped plate. Solid line and dotted line show the results of the experiment, and of the simulation, respectively. In the case of the plate without the damper, it is clear that the plate has high Q-value. Sound pressure level of sound field may be greatly changed at resonant frequency. On the other hand, frequency characteristics of sound pressure level became flat when the plate was damped. In addition, clay is pasted on a plate as the damper to prevent causing standing wave in the experiment as shown in Fig. 4.4(g). The shape of clay is defined in order that resonant characteristics of the plate with clay in the experiment is similar to that of the damped plate in the simulation. According to Fig. 4.4(g), the evanescent sound field was generated without nodes as is the case

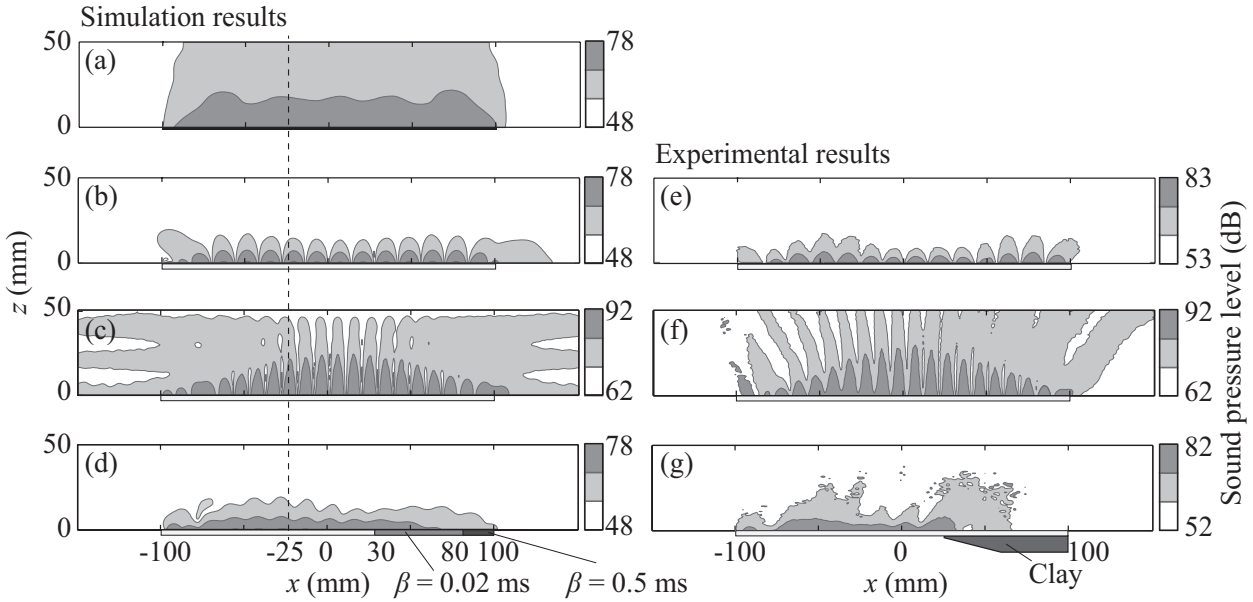


Figure 4.4: Sound pressure level of the sound field on $xz$-plane: (a) driving frequency $f$ = 10 kHz in the case of piston sound source, (b) $f$ = 10 kHz, (c) $f$ = 20 kHz, (d) $f$ = 10 kHz in the case of damped plate in the simulation. (e) $f$ = 10 kHz, (f) $f$ = 20 kHz, (g) $f$ = 10 kHz in the case of damped plate in the experiment.

in Fig. 4.4(e). It is preferable that frequency characteristics of sound are flat in data communication when modulation method such as OFDM is used. In the proposed acoustic transducer, it is clear that frequency band of 8 – 15 kHz meets the conditions; frequency characteristics are flat and the evanescent sound field can be generated. Acoustic data signal could be received by the microphone attached to mobile devices in this audio frequency band. However, group delay difference which is caused by the dispersion of phase and group velocities is a shortcoming with the proposed acoustic transducer. For realization of the near-field acoustic communication, there is a need to determine if group delay difference influence the availability of data communication.

## 4.3 Communication quality of near-field acoustic communication system

### 4.3.1 Influence of group delay difference for acoustic communication

Communication quality of near-field acoustic communication system is investigated. We look at the effect of group delay difference on acoustic communication. In the case of vibration plate made from a homogeneous plate, group delay difference is caused with respect to frequency because phase velocity of the flexural wave has dispersion as shown in Fig. 2.2. Therefore, we attempt to calculate the group delay difference in frequency band 8 – 15 kHz which was considered appropriate for data communication in previous subsection. Figure 4.7 shows frequency characteristics of group delay time $T_g$ at edge of the proposed acoustic transducer (($x$, $z$) = (100, 0) in Fig. 4.4) was calculated. Here, group delay time difference $\Delta T_g$ at the re-

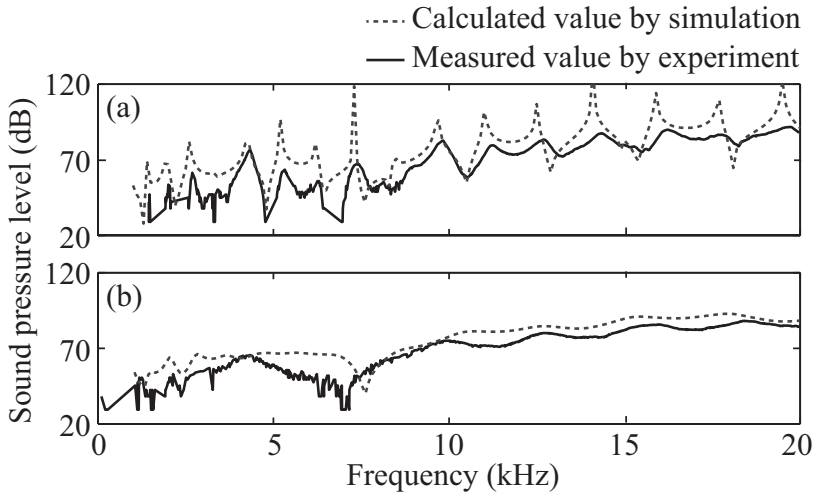


Figure 4.5: Frequency characteristics of sound pressure level at ($x$, $z$) = (-25, 0) in the simulation and experiment: (a) without the damper and (b) with the damper.

ceiving point is expressed as following equation using group delay time $T_g$ at edge of the proposed acoustic transducer (($x$, $z$) = (100, 0) in Fig. 4.4) because of its monotonically decreasing in the proposed acoustic transducer.

$$\Delta T_g = |T_g(f_{c\,max}) - T_g(f_{c\,min})|. \tag{4.1}$$

Where $f_{c\,max}$ and $f_{c\,min}$ are maximum and minimum frequency of carrier wave, respectively. Figure 4.8 shows outline of transmitting signal and receiving signal that has delay time with respect to frequency. Multicarrier modulation method such as OFDM has a property of maximum tolerable delay time difference $\tau = 1/\Delta f_c$; $\Delta f_c$ is frequency bandwidth of carrier wave. Demodulation is difficult in basic OFDM system when $\Delta T_g > \tau$. According to group velocity calculated using phase velocity shown in Fig. 2.2, $\Delta T_g$ = 0.107 ms and $\tau$ = 0.143 ms when frequency band is 8 – 15 kHz. It is clear that delay time difference in the proposed acoustic transducer is insignificant for data communication. If vibration plate is longer and frequency bandwidth is wider, $\Delta T_g$ becomes large and $\tau$ becomes small. Therefore, it is preferable that we choose the vibration plate whose phase velocity has small dispersion. From these results, it was confirmed that acoustic data can be received at any point near the plate by mobile devices since sound is generated with uniform level and small time delay. Therefore, the proposed acoustic transducer can be utilized as an near-field acoustic data generator for mobile devices.

### 4.3.2 Receivable distance of near-field acoustic communication system

Receivable distance of acoustic data is compared. We assumed that the near-field acoustic communication system using the proposed acoustic transducer can be generate sound whose maximum level is 20 dB larger at the surface of the acoustic transducer than noise level emanating around the system. Carrier-noise ratio (CNR) at $x$ = 25 mm in the simulation is obtained using the distribution of sound pressure level shown in Fig. 4.4. Here, the bit error rate (BER) in the binary phase-shift keying (BPSK) as a function of the $E_b/N_0$

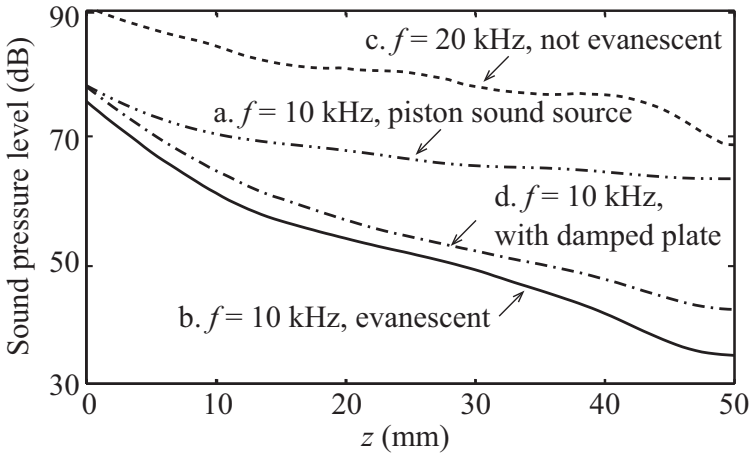


Figure 4.6: Sound pressure level at $x$ = -25 mm in the simulation.

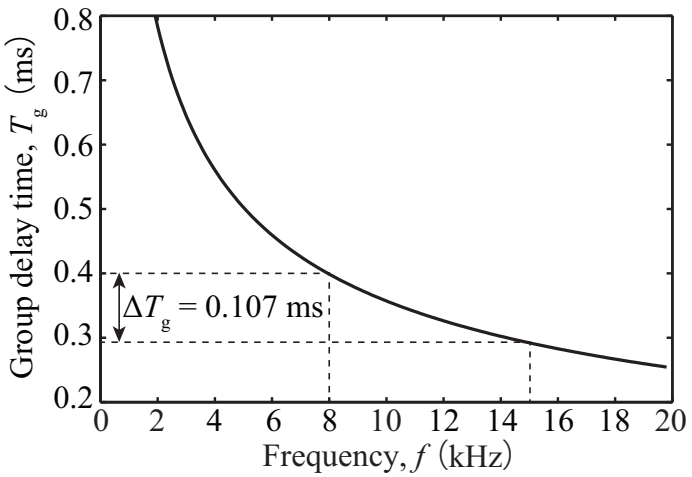


Figure 4.7: Frequency characteristics of group delay time at edge of the proposed acoustic transducer (($x$, $z$) = (100, 0) in Fig. 4.4).

(energy per bit to noise power spectral density ratio) is given by following equation,

$$p_{\mathrm{e}} = \frac{1}{2}\mathrm{erfc}\left(\sqrt{\frac{E_{\mathrm{b}}}{N_0}}\right), \tag{4.2}$$

where erfc is the error function.[46] $E_{\mathrm{b}}/N_0$ is obtained for the product of CNR and the link spectral efficiency of a digital communication system. The link spectral efficiency is 1 when near-field acoustic communication which is proposed as a digital modulation method based on orthogonal frequency-division multiplexing (OFDM) is used. Therefore, $E_{\mathrm{b}}/N_0$ is equivalent to CNR. Figure 4.9 shows the BER in $x$ = 25 mm obtained by substituting CNR into Eq. (4.2). The horizontal axis shows the distance from the surface of the plate, and the vertical axis shows the BER. Curves a, b, c, and d correspond to sound pressure level when $f$ = 10 and 20 kHz, $f$= 10 kHz in the case of damped plate and $f$ = 10 kHz in the case of piston sound source,

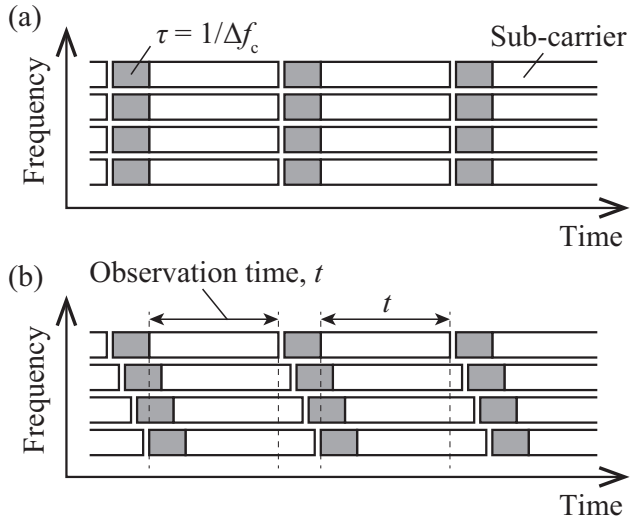


Figure 4.8: Outline of transmitting signal and receiving signal: (a) transmitting signal and (b) receiving signal that has delay time with respect to frequency.

respectively. In general, it is described that the data communication is available when the BER is under 0.01. According to the curves a and c in Fig. 4.9, these BERs are under 0.01 until $z$ = 45 mm. On the other hand, according to the curves b and d in Fig. 4.9, these BERs are under 0.01 during $0 \leq z \leq 12$ mm. It is clear that the proposed acoustic transducer can limit the distance receiving acoustic data signal. Also, in the case of the plate without the damper shown by the curves b and c in Fig. 4.9, these BERs become high at the position of nodes in the sound field shown by the curves b and c in Fig. 4.9. On the other hand, in the case of the proposed acoustic transducer with the damper, difference of the BER depends only on the distance from the surface of the plate since its evanescent sound field is uniform, as shown in Fig. 4.4(d). Therefore, the damper needs to attach on the proposed acoustic transducer to attenuate flexural wave at the end of the plate.

### 4.3.3 Leakage of non-evanescent sound field

We examine the root cause of sound wave leakage from the proposed acoustic transducer. The proposed acoustic transducer can increase the data transmission speed using a wide frequency band including auditory frequencies because the generated sound does not reach the audible spatial area in theory. However, a discontinuity of the sound field exists at the edge of the finite vibration plate in practice. This increases the extent of the wavenumber spectrum, and the vibration plate fails to satisfy the condition of $k_{\mathrm{p}} > k$. In consequence, a sound wave radiates over the evanescent sound field, causing the leakage of acoustic data and sound noise. Therefore, we need a method for reducing the extent of the wavenumber spectrum or a vibration plate that always satisfies the condition of $k_{\mathrm{p}} > k$. Since the proposed acoustic transducer consists of a homogeneous vibration plate, $k_{\mathrm{p}}$ can be increased by reducing the thickness or by choosing a material that has a high density and low Young's modulus. However, the area in which data communication can be performed becomes extremely narrow because the attenuation of the sound pressure with increasing distance

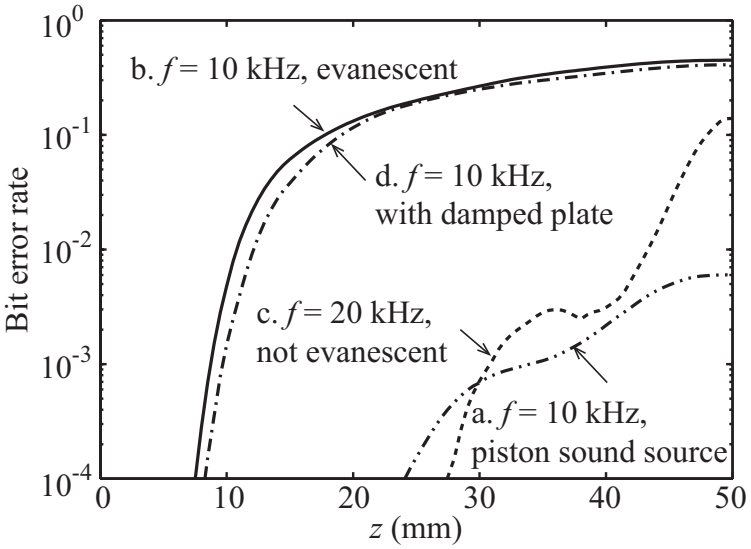


Figure 4.9: Bit error ratio at $x$ = -25 mm in the simulation.

from the surface of the vibration plate becomes too large with increasing $k_{\mathrm{p}}$. Accordingly, we must consider the use of near-field acoustic communication.

Figure 4.10 shows the wavenumber spectrum of a flexural wave propagating on an infinite vibrating plate with the wavenumber $k_{\mathrm{p}}$ and that obtained by applying a finite rectangular window to the particle velocity field. The solid line and dashed line show the results for the infinite vibrating plate and finite rectangular window, respectively. In the case of the infinite vibrating plate, only the component with the wavenumber $k_{\mathrm{p}}$ exists in the particle velocity field, and no extra components of the wavenumber spectrum, called spurious signals, appear. Thus, the evanescent wave dominates the sound field. On the other hand, in the case of the finite rectangular window, the wavenumber spectrum has a main lobe with a finite bandwidth and the spurious signal is large. Additionally, a non-evanescent sound wave radiates since a large power exists at wavenumbers smaller than $k$, the wavenumber of a plane wave in air. Therefore, the window function is necessary for suppressing sound leakage and securing a spatial area for data communication.

Here, we discuss the window functions used in this study and their characteristics. We use a triangular window, a Hann window, a cosine window, and a Blackman window. Figures 4.12 and 4.13 respectively show the window functions and their wavenumber spectra. The solid line, dashed line, chain line, and two-dot chain line in Fig. 4.12 show the triangular window, Hann window, cosine window, and Blackman window, respectively. It is confirmed that the triangular window and cosine window have a large side lobe level. However, the main lobe of the cosine window is the narrowest. The width of the main lobe of the Hann window is identical to that of the triangular window. Nevertheless, the spurious level of the Hann window is lower than that of the triangular window. On the other hand, the Blackman window has the smallest spurious level and the widest main lobe. Since these windows have different characteristics, optimization calculation is necessary to determine the window function most suitable for data communication. Figure 4.11 shows an example of a window function with a shoulder part consisting of a cosine roll-off. This window is called the cosine roll-off window. The window function is optimized by varying the ratio of the shoulder part to the

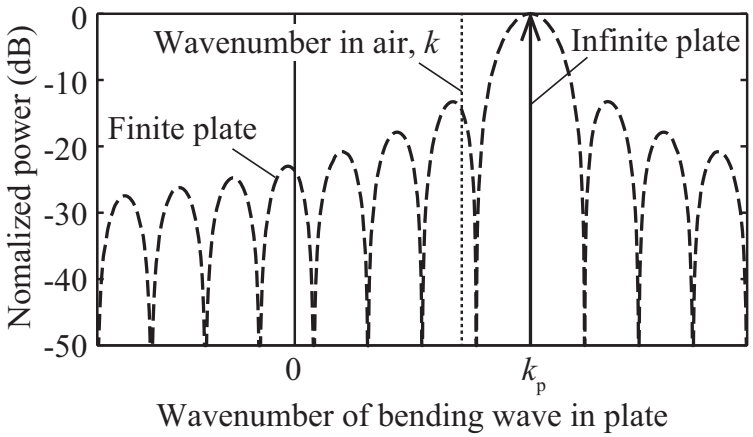


Figure 4.10: Wavenumber spectrum of the flexural wave propagating on an infinite vibrating plate with wavenumber $k_{\mathrm{p}}$ and that obtained applying a finite rectangular window to the particle velocity field.

flat part of the window, as shown in Fig. 4.11. To secure a large sound pressure level in the receivable area, the minimum value of the window inside the receivable area is unity.

In addition, it is predicted that the sound pressure level of a sound wave leaking to a far field changes with the ratio of $k_{\mathrm{p}}$ to $k$. We have to take into account the fact that the wavenumber $k_{\mathrm{p}}$ is defined as a function of the frequency in the case of the vibrating plate, as shown in Fig. 2.2. Therefore, we calculate the variation of the sound pressure level at the far field with respect to the frequency and window shape. Calculation methods for the sound pressure level at the far field from a vibrating plate are investigated.

## 4.4 Suppression of sound wave leakage using optimization of window function

### 4.4.1 Calculation of sound pressure level at far field of vibration plate

We investigated calculation methods of sound pressure level at far field from a vibration plate. First, we used a calculation method of sound pressure level at the finite distance from the vibration plate, as a realistic method. Acoustic holography is well-known as a method for calculating sound field on a plane using another sound field on parallel plane. The acoustic holography can be utilized for the evaluation of the difference of sound pressure level between an adjacent surface of the vibration plate and a parallel surface at a distance from the vibration plate. However, we should consider about sound wave radiating at an angle given by Eq. (3.6) when the wavenumber $k_{\mathrm{p}}$ of the flexural wave is smaller than the wavenumber $k$ of plane wave in air. The calculation surface at far field for evaluating all of sound radiation in a finite length is not on the parallel plane but a spherical surface. Therefore, we used Rayleigh integral that can calculate sound pressure at any observation point.[47] Figure 4.14 shows the position of the vibration plate of the proposed acoustic transducer on the $xy$-plane, and the calculation area of sound pressure level at far field. The length $L$ of the vibration plate was 200 mm. The calculation area, which disallows data communication, was defined outside of semicircle of radius 500 mm that was far enough from the center of the vibration plate.

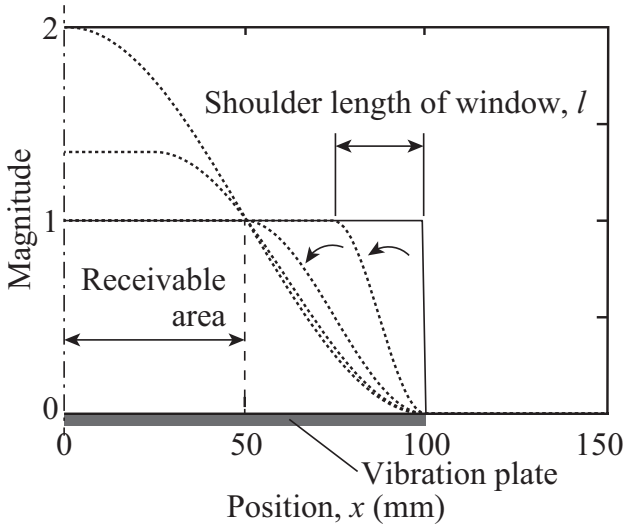


Figure 4.11: Example of the window function that has the shoulder part consisting of cosine roll-off.

The boundary of the calculation area was called the evaluation boundary. The calculation interval on the evaluation boundary was tenth part of the maximum wave length $\lambda$ of radiated sound. It was assumed that the proposed acoustic transducer, which was surrounded by an infinite baffle at $z = 0$, vibrated with flexural wave at particle velocity $v(x, t)$. Additionally, particle velocity distribution of the $y$-direction was assumed to be uniform within the range of the width of the vibration plate. When sound pressure radiated from a point $\boldsymbol{r_0} = (x_0, y_0, z_0)$ on the vibration plate is observed at a point $\boldsymbol{r} = (x, y, z)$, velocity potential $\phi(\boldsymbol{r})$ in harmonic analysis is indicated as following equation.

$$\phi(\boldsymbol{r}, t) = \iint_S \frac{1}{2\pi\,|\boldsymbol{r} - \boldsymbol{r_0}|} v\left(t - \frac{|\boldsymbol{r} - \boldsymbol{r_0}|}{c}\right) dx_0 dy_0, \tag{4.3}$$

$$v\left(t - \frac{|\boldsymbol{r} - \boldsymbol{r_0}|}{c}\right) = u_{\mathrm{p}} \exp\left(-jk_{\mathrm{p}}x\right) \exp\left[j\omega\left(t - \frac{|\boldsymbol{r} - \boldsymbol{r_0}|}{c}\right)\right]. \tag{4.4}$$

The following equation that separated $\exp(j\omega t)$ from Eq. (4.4) was utilized so as to perform harmonic analysis in this study.

$$\phi(\boldsymbol{r}) = \iint_S \frac{1}{2\pi\,|\boldsymbol{r} - \boldsymbol{r_0}|} u_{\mathrm{p}} \exp\left(-jk_{\mathrm{p}}x\right) \exp\left[-j\omega\frac{|\boldsymbol{r} - \boldsymbol{r_0}|}{c}\right] dx_0 dy_0, \tag{4.5}$$

where $S$, $c$ and $u_{\mathrm{p}}$ are the total area of the vibration surface, sound velocity of plane wave in air and the amplitude of flexural vibration, respectively. The calculation intervals in the $x$- and the $y$-directions on the vibration surface were hundredth part of the maximum wave length $\lambda_{\mathrm{p}}$ and tenth part of $\lambda_{\mathrm{p}}$ of the flexural wave.

Next, we also investigated a calculation method of sound pressure level at infinite field. The method employs the Frounhofer approximation to define the wavenumber spectrum of a vibrating surface as the sound pressure level at an infinite far field.[48] The wavenumber spectrum was calculated by performing a Fourier transform with respect to the distribution of the sound pressure on the vibrating plate. The sound

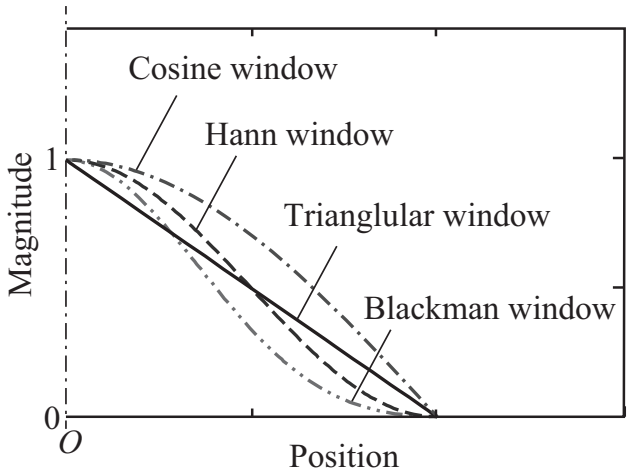


Figure 4.12: Window functions: triangular window, Hann window, cosine window, and Blackman window.

wave radiating at an angle given by following equation when the wavenumber $k_{\mathrm{p}}$ of the flexural wave is smaller than the wavenumber $k$ of plane wave in air. Therefore, the sound pressure level at the angle of an infinite distance was calculated by converting the wavenumber $k_{\mathrm{p}}$ into the angle using Eq. (3.6). The region of the vibrating plate and the calculation area on the $x$-axis were -100≤$x$≤100 mm and -1,000≤$x$≤1,000 mm, respectively. The calculation interval was $\lambda_{\mathrm{p}}/100$.

In both methods, we compared between sound pressure level at far field under the condition generating evanescent sound field, i.e., $k_{\mathrm{p}} > k$ and that under the condition radiating sound wave, i.e., $k_{\mathrm{p}} < k$. Therefore, flexural wave propagating in 6 and 30 kHz on the acrylic plastic plate shown in Fig. 2.4 was assumed.

We compared the distributions of sound pressure level at the finite distance and infinite field from the vibration plate. The $z$-axis was set standard as 0 rad. Sound pressure level was normalized using the maximum value in a range from $-\pi/2$ to $\pi/2$. Figures 4.15(a) and 4.15(b) show the angular characteristics of sound pressure level in 6 and 30 kHz frequency, respectively. The solid line and the dotted line show sound pressure level on the evaluation boundary and that obtained at infinite field.

In the case of $f$ = 6 kHz under the condition of generating evanescent sound field, the angular characteristics of sound pressure level at the finite distance was in good agreement with that of infinite field, as shown in Fig. 4.15(a). In addition, sound pressure level differences with respect to angle were small. On the other hand, in the case of $f$ = 30 kHz under the condition of radiating sound wave, sound pressure level at infinite field had maximum value with a sharp peak at $\pi/4$. Level difference between the maximum value of the main lobe and that of an adjacent peak was approximately 13 dB. Sound pressure level on the evaluation boundary also had maximum value at $\pi/4$, however, the main lobe was wider than that of infinite field. It is inferred that the sound wave is radiated similarly to a beam from the finite vibration plate, and the beam width was not short enough with respect to the perimeter of the semicircle of the evaluation boundary, as shown in Fig. 3.2(a). Consequently, sound pressure level on the evaluation boundary was in disagreement with that obtained at infinite field.

We aim to design the window function that reduces the maximum sound pressure level at far field for

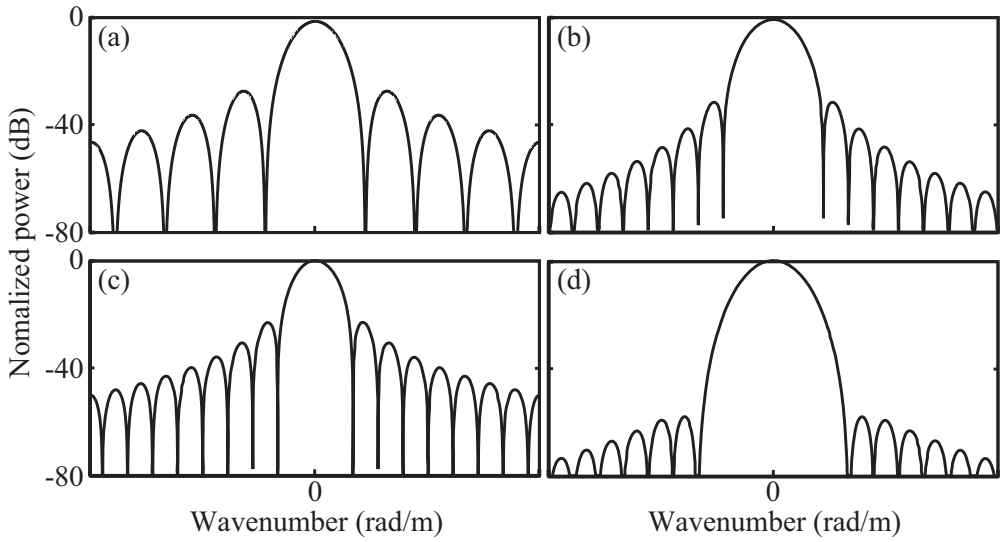


Figure 4.13: Wavenumber spectra of window functions: (a) triangular window, (b) Hann window, (c) cosine window, and (d) Blackman window.

suppressing leaking sound wave. Therefore, the error at the dip shown in Fig. 8 is not going to matter as much when the peak values of both methods are identical. According to Fig. 4.15(a), the differences of the level and the position at the peak between the case of the finite distance and that of infinite field would not be caused under the condition of generating evanescent sound field. Additionally, the method using the wavenumber spectrum on the vibration plate can calculate easily compared to that using Eq. (4.5). Since this study aims to suppress the radiation component of evanescent sound field, we evaluate sound pressure level at far field using the method that calculates the wavenumber spectrum on the vibration plate.

### 4.4.2 Frequency characteristics of sound pressure level with respect to window shape

The distribution of particle velocity has to be designed to suppress sound pressure level at far field. Therefore, sound pressure level at far field from the vibration plate with respect to frequencies and window shapes is calculated. Here, we set some limiting conditions for the window function that determine the distribution of particle velocity of the vibration surface. First, the entire length of the window function was identical to the length of the vibration plate of the proposed acoustic transducer, i.e., $L$ = 200 mm. The window function was symmetry at the center of the vibration plate. Next, ratio of the shoulder part and the flat part of the window were changed by varying the shoulder length $l$ from 0 to 100 mm. In addition, it was inferred that sound pressure level at the receivable area above the vibration plate becomes small by increasing the ratio of the shoulder. Therefore, the area where the data should reach was defined as a range -50$\leq x \leq$50 mm, and the minimum value of the window inside the area was set as 1. Additionally, the window functions that have the shoulders consisted of the triangular window, the Hann window, the cosine window, and the Blackman window are called triangular-type window, cosine roll-off window, cosine-type window, and Blackman-type window, respectively. Maximum value of sound pressure level within a range under the condition of radi-

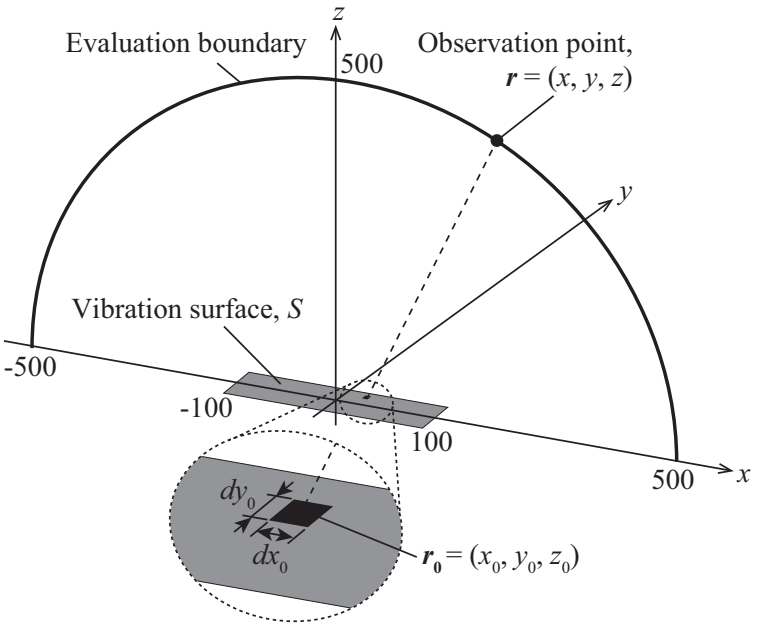


Figure 4.14: Position of the vibration plate of the proposed acoustic transducer on the $xz$-plane, and the calculation area of sound pressure level at far field.

ation sound $k_{\mathrm{p}} < k$ was obtained by calculating the wavenumber spectrum on the vibration plate when the window functions were given to the particle velocity field. Finally, we require consideration of the fact that the proposed acoustic transducer was designed for data communication intended for mobile devices. Therefore, frequency characteristics of sound pressure level was calculated in the frequency band $1 \leq f \leq 15$ kHz that was under the condition of generating evanescent sound field theoretically and can be received by the microphone attached in mobile devices. The calculation interval of frequency was 0.1 kHz.

Figure 4.16 shows sound pressure level at far field from the vibration plate with respect to frequencies and window shapes. Figures 4.16(a), 4.16(b), 4.16(c), and 4.16(d) show the results of the triangular-type window, the cosine roll-off window, the cosine-type window, and the Blackman-type window, respectively. In addition, it is clear from Figs. 4.16(a) – 4.16(d) that sound pressure level increased at approximately $f$ = 10 kHz. The frequency band under 15 kHz meets the condition of generating evanescent sound field theoretically when the vibration surface has infinite length. However, it was inferred that the main lobe of the wavenumber spectrum increased in width owing to cutting the length off finitely in all windows. Therefore, the part of the main lobe already existed in the area smaller than the wavenumber $k$ of the plane wave in air at $f$ = 10 kHz. For the fact that sound pressure level of radiated sound is large in all windows, it was indicated that the frequency band over $f$ = 10 kHz is unsuitable for limiting the communication area near the proposed acoustic transducer. In addition, the maximum sound pressure level at far field was changed depending on frequency, the length of the shoulder, and the types of the windows. The window function, in which the maximum sound pressure level is small, has to be designed for suppressing sound leakage. However, the proposed acoustic transducer aims to transmit acoustic data with wide-bandwidth of frequency to permit high-data transmission speeds. It is also necessary to prevent sound from radiating at

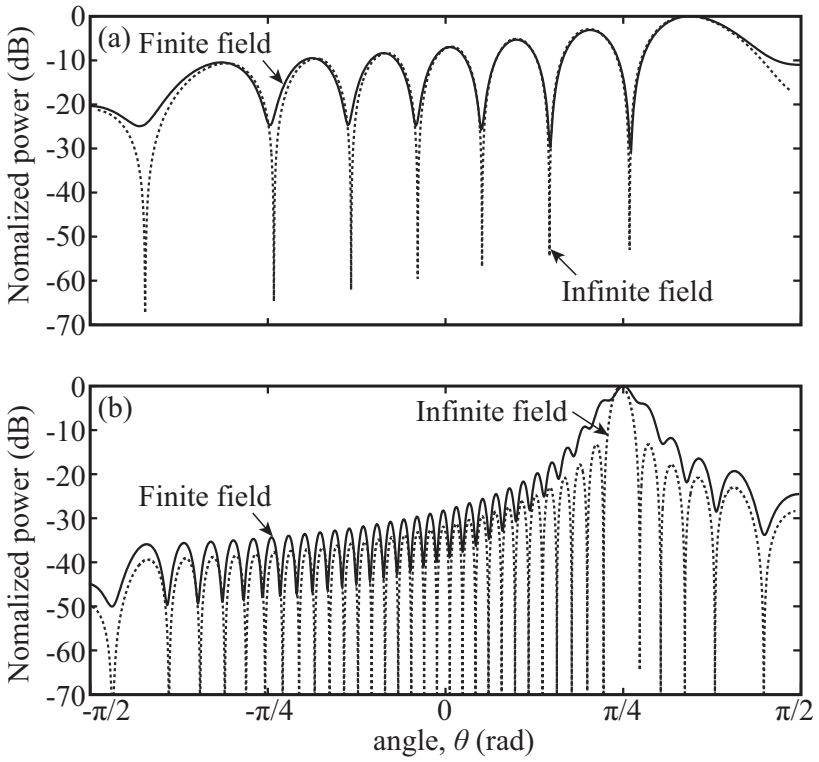


Figure 4.15: Angular characteristics of sound pressure level in frequency (a) $f$ = 6 kHz and (b) $f$ = 30 kHz.

specific frequency so as not to leak out sound noise as well as acoustic data. Therefore, we optimize the window function in the frequency band $1 \leq f \leq 10$ kHz so that the maximum sound pressure level at far field becomes the smallest.

### 4.4.3 Procedure of optimization of window function

The limiting conditions in the optimization of the window function follow those in the previous section. Here, we describe the evaluation function use in the optimization. Similarly, the sound pressure level was calculated using the wavenumber spectrum on the vibrating surface by the same method as that in the previous section. The maximum sound pressure level of the radiated sound at the infinite far field from the vibrating plate was calculated. The window function in which the maximum sound pressure level at the far field has the smallest value in the frequency band $1 \leq f \leq 10$ kHz was obtained. Under these conditions, the optimization involves the following steps.

(1) The maximum sound pressure level $L_{\max}$ at an infinite far field in the frequency band $1 \leq f \leq 10$ kHz for each shoulder length in the range of $0 \leq l \leq 100$ mm is calculated.

(2) The shoulder length of the optimal window that gives the minimum value of $L_{\max}$ in step (1) is searched for.

Using the evaluation function, the optimized window that suppresses sound leakage at the far field when using the proposed acoustic transducer for data communication was determined.

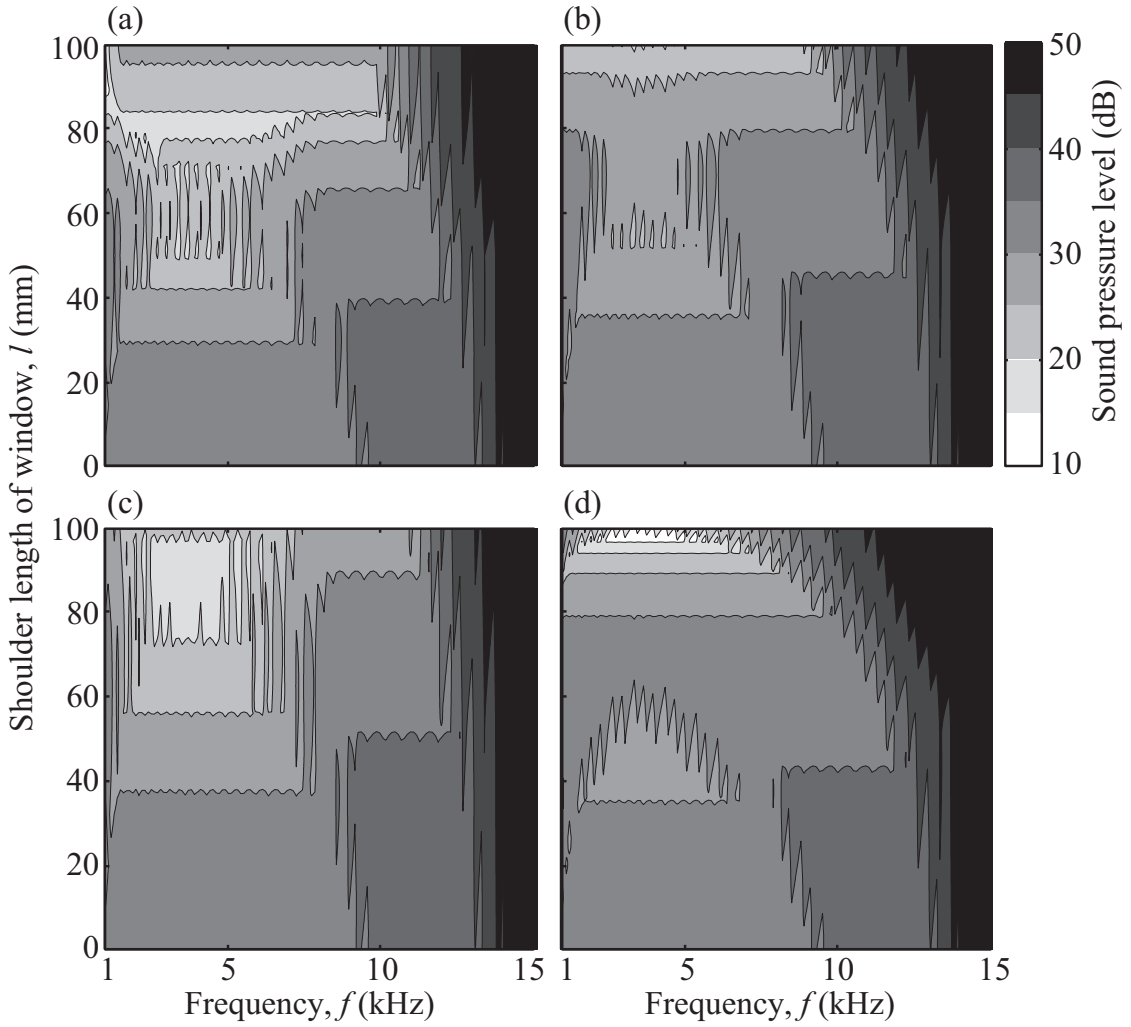


Figure 4.16: Sound pressure level at the far field from the vibrating plate with respect to the frequency for the (a) triangular-type window, (b) cosine roll-off window, (c) cosine-type window, and (d) Blackman-type window.

### 4.4.4 Results and discussion

Figure 4.17 shows $L_{\max}$ with respect to the shoulder length of the window in the frequency band $1 \leq f \leq 10$ kHz. The solid line, the dashed line, the chain line, and the two-dot chain line show $L_{\max}$ of the triangular-type window, the cosine roll-off window, the cosine-type window, and the Blackman-type window. The shoulder lengths, which took the minimum value of $L_{\max}$ of the triangular-type window, the cosine roll-off window, the cosine-type window, and the Blackman-type window, were 80, 84, 100, 74 mm, as shown in Fig. 4.17. The corresponding values of $L_{\max}$ were 17.22, 22.75, 22.11, and 25.35 dB, respectively. Thus, the triangular-type window with $l$ = 80 mm, for which the minimum value of $L_{\max}$ was obtained among the four types of windows, was determined as the optimized window.

The distribution of sound pressure level at the $xz$-plane ($y$ = 0) was calculated using Rayleigh integral to confirm that the sound pressure level varies depending on the presence or absence of the optimized window.

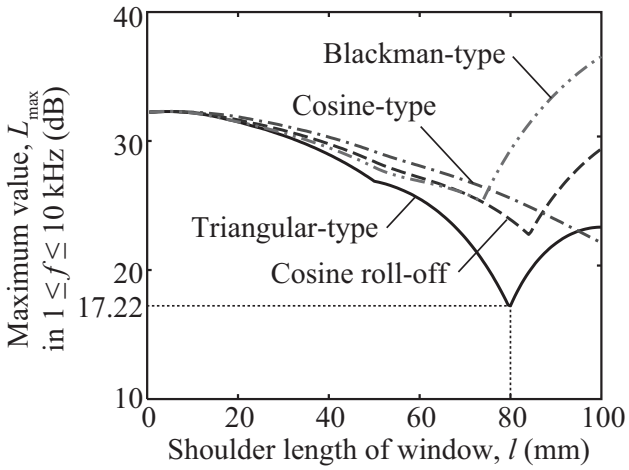


Figure 4.17: Maximum value $L_{\max}$ with respect to the edge length of the window in the frequency band $1 \leq f \leq 10$ kHz.

The calculation intervals in the $x$- and $y$-directions on the vibrating surface were one-hundredth of the maximum wavelength $\lambda_{\mathrm{p}}$ and one-tenth of $\lambda_{\mathrm{p}}$ for the flexural wave. The calculation area in the sound field was -500$\leq x \leq$500 mm and 0$\leq z \leq$1,000 mm. The calculation interval was 1 mm. Figure 4.18 shows the distribution of sound pressure level at the $xz$-plane ($y$ = 0). Figs. 4.18(a) and 4.18(b) show the distribution of sound pressure level without and with the optimized window in $f$ = 6 kHz, respectively. The maximum sound pressure level in each sound field was normalized as 0 dB, and the level was shown until -50 dB.

First, we focused on the area whose level was in the range from 0 to -10 dB. According to Figs. 4.18(a) and 4.18(b), this area was included within the area -50$\leq x \leq$50 mm. This suggests that a sufficiently high sound pressure level can be secured within the area defined as the minimal spatial area for data communication. Next, we focused on the sound pressure level at the far field. In the case without the optimized window, the area where the sound pressure level decreased from -40 to -50 dB existed at $z$ = 1,000 mm, as shown in Fig. 4.18(a). On the other hand, in the case with the optimized window, the area where sound pressure level decreased from -40 to -50 dB existed within -150$\leq x \leq$500 mm and 0$\leq z \leq$250 mm, as shown in Fig. 4.18(b).

It was predicted that the Blackman window is the most effective for suppression of sound leakage in the case of a single frequency since the spurious of the wavenumber spectrum is the smallest. However, the acoustic transducer using evanescent sound field has been proposed for near-field acoustic communication transmitting the acoustic data with a frequency bandwidth. Therefore, we had to secure large level in a receivable area as well as to suppress sound wave leakage. The results indicated that large sound pressure level can be secured within the area that was defined as the minimal spatial area for data communication. The sound pressure level decreased in a shorter distance than in the case without the optimized window. Therefore, it is possible to design an optimized function using the evaluation function and to limit the area that transmits acoustic data using the optimal window while securing a high sound pressure level near the vibrating plate. According to these results, near-field acoustic communication with suppressed sound leakage can be achieved by applying the optimal window to the particle velocity field.

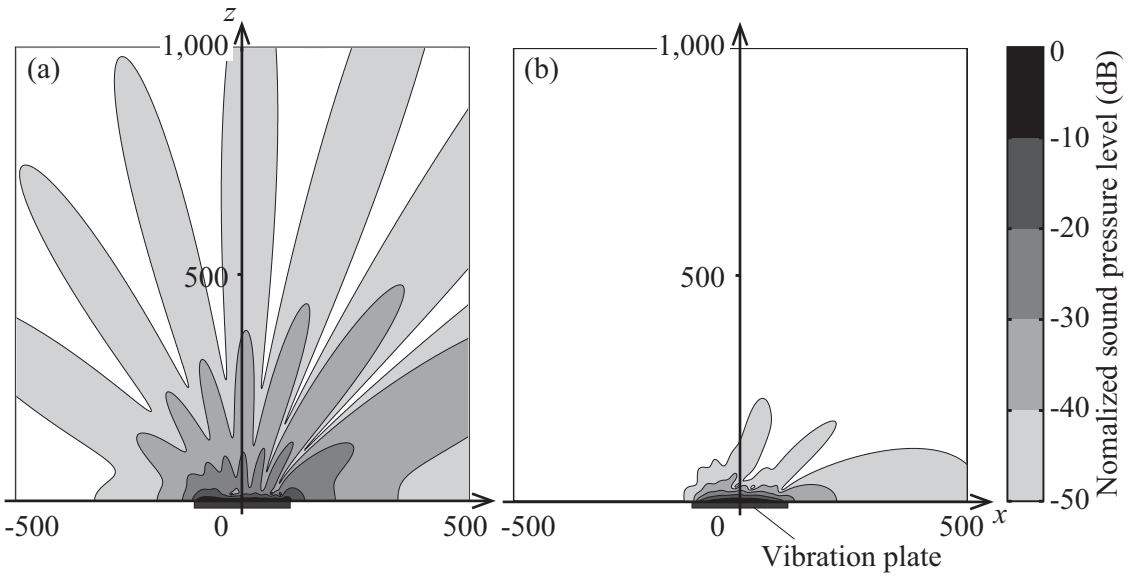


Figure 4.18: Distribution of sound pressure level on the $xz$-plane ($y = 0$) (a) without optimized window and (b) with optimized window.

## 4.5 Shading of sound source using porous material to suppress sound leakage

### 4.5.1 Acoustic characteristics of porous material

To confirm the feasibility of distributing the particle velocity field in reality, we simulate the particle velocity above the vibration surface when a sound insulator made of porous material is put into the evanescent sound field. Porous materials are often used for sound absorption and insulation. The characteristic impedance $Z$ and propagation constant $\gamma$ of a porous material are expressed as the following functions of the flow resistivity $R_\mathrm{f}$ and frequency $f$ in the Miki model:[49,50)]

$$Z(f) = R(f) + jX(f), \tag{4.6}$$

$$\gamma(f) = \alpha(f) + j\beta(f), \tag{4.7}$$

$$R(f) = \rho c \left[1 + 0.070 \left(\frac{f}{R_\mathrm{f}}\right)^{-0.632}\right], \tag{4.8}$$

$$X(f) = -0.107\rho c \left(\frac{f}{R_\mathrm{f}}\right)^{-0.632}, \tag{4.9}$$

$$\alpha(f) = \frac{\omega}{c}\left[0.160 \left(\frac{f}{R_\mathrm{f}}\right)^{-0.618}\right], \tag{4.10}$$

$$\beta(f) = \frac{\omega}{c}\left[1 + 0.109 \left(\frac{f}{R_\mathrm{f}}\right)^{-0.618}\right], \tag{4.11}$$

where $c$ and $\omega$ are the sound velocity in air and the angular frequency, respectively.

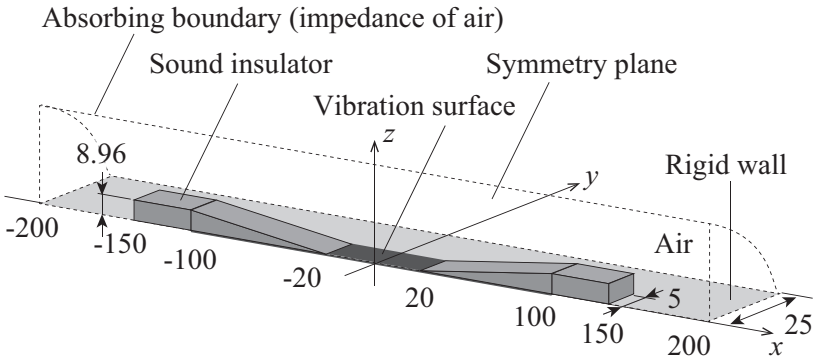


Figure 4.19: Shape of the sound insulator along with the sound field and boundary conditions in the simulation using the three-dimensional FEM.

### 4.5.2 Simulation using finite element method

Here, the distribution of the particle velocity in the case that a porous material, as an example of a sound insulator, is placed above the vibrating surface was calculated by FEM simulation. The evanescent sound field was generated by interchanging the normal particle velocity of a flexural wave traveling in the positive $x$-direction on the vibrating surface and that of the sound field. The pressure of the sound field was input into the vibrating surface. The flexural wave was assumed to be propagating with a frequency of $f = 6$ kHz on the acrylic plate in accordance with Fig. 2.2. The shape of the sound insulator should be designed so that the distribution of the particle velocity above the sound insulator is extremely close to that obtained using the optimized window function. However, the attenuation characteristics in the porous material have not been analyzed in detail when the material is placed in the evanescent sound field. On the other hand, it is well known that the amplitude decreases with increasing thickness of the porous material in the case of a plane wave. Therefore, we investigate the possibility of distributing the particle velocity above the vibrating surface using a sound insulator with a continuous thickness distribution. The sound insulator had a wedge shape so that the distribution of the particle velocity at the edge of the vibrating surface changes smoothly. Figure 4.19 shows the shape of the sound insulator along with the sound field and boundary conditions in the simulation. Since the sound field, vibrating surface, and sound insulator were symmetric with respect to the $xz$-plane, only one side of the symmetry plane was simulated so as to reduce the computational cost. Therefore, the widths of the vibrating surface and sound insulator were 5 mm, i.e., half the width of the proposed acoustic transducer. The length of the vibrating surface was identical to the length $L$ of the proposed acoustic transducer. The flow resistance $R_\mathrm{f}$ of the sound insulator, assumed to be rock wool, was $1\times10^6$ Pa·s/m$^2$, and the characteristic impedance and propagation constant of the porous material were calculated using Miki model. The maximum thickness of the sound insulator was 8.96 mm, which was one-quarter of the wavelength of the flexural wave when $f = 6$ kHz. In addition, the slope length of the sound insulator was 80 mm. The boundary of the sound field was assumed to satisfy the absorbing boundary condition. The vibrating surface was surrounded by a rigid wall. The distribution of the particle velocity at a distance of 1 mm from the sound insulator ($z = 9.96$ mm) was calculated.

### 4.5.3 Results and discussion

Figure 4.20 shows the distributions of the particle velocity at a distance of 1 mm from the sound insulator ($z$ = 9.96 mm) when $f$ = 6 kHz. Figures 4.20(a) and 4.20(b) show the distributions of the particle velocity obtained without and with the sound insulator, respectively. The particle velocity at the flat part was normalized as 1. The solid line and dashed line respectively show the ideal value obtained using the Rayleigh integral in the previous section and the simulation result obtained by FEM simulation. The chain line shown in Fig. 4.20(b) shows the result obtained by FEM simulation in the case of inputting the optimized function in the vibrating surface. The chain line cannot be seen because it is in exact agreement with the solid line obtained using the Rayleigh integral. In addition, in the result obtained without the sound insulator, the distribution of the particle velocity at $z$ = 9.96 mm was in good agreement with the ideal value in that the particle velocity increased at the edge of the vibrating plate, as shown in Fig. 4.20(a). The results suggest that it is appropriate to calculate the distribution of the particle velocity by FEM simulation. From Figs. 4.20(a) and 4.20(b), it can be seen that the distribution of the particle velocity was asymmetric regardless of the presence of the sound insulator because the phase of the vibrating surface was also asymmetric. In the result obtained with the sound insulator, the right part of the slope was in good agreement with the ideal value, as shown in Fig. 4.20(b). However, only the left part of the slope increased rapidly despite the symmetry of the sound insulator. The increase in particle velocity was presumably due to the interference of the leaking wave from the edge of the vibrating surface and from the thin part of the sound insulator. According to these results, even if a symmetric sound insulator is placed in the evanescent wave field, it cannot produce a symmetric distribution of the particle velocity field.

Furthermore, the sound radiation from the vibrating surface with the distribution of the particle velocity shown in Fig. 4.20(b) was obtained using the Rayleigh integral. Figure 4.21 shows the distributions of the sound pressure level on the $xz$-plane when $f$ = 6 kHz. Figures 4.21(a) and 4.21(b) show the simulation results obtained with the optimized window and with the sound insulator, respectively. The maximum sound pressure level in each sound field was normalized as 0 dB, and the sound pressure level was shown down to -50 dB. It can be seen that the sound field obtained by the sound insulator shown in Fig. 4.21(a) was in good agreement with that shown in Fig. 4.18(b). On the other hand, the suppression effect of the sound insulator seems to be small in comparison with the optimized window function in this simulation as shown in Figs. 4.21(a) and 4.21(b). Nevertheless, the area where the sound pressure level decreased from -30 to -50 dB was limited in comparison with the result obtained without the sound insulator shown in Fig. 4.18(a).

According to the results, it was clarified that the sound insulator can control the distribution of the particle velocity via its thickness distribution. In addition, it was suggested that a sound insulator made of a porous material can suppress sound leakage by placing it above the vibrating plate. However, the sound insulation characteristics vary intricately with the physical properties of the porous material, such as the density, the diameter of the fibers, and the percentage volume of air pores. Therefore, the attenuation characteristics of the evanescent sound field in the porous material should be analyzed in more detail. For this reason, it remains a challenge to propose a theoretical method for calculating the shape of a sound insulator that gives an identical distribution to the window function optimized by the evaluation function. To further verify the applicability of the evaluation function for calculating the optimized window function, we plan to propose a theoretical equation for calculating the shape of the sound insulator using the optimized window function

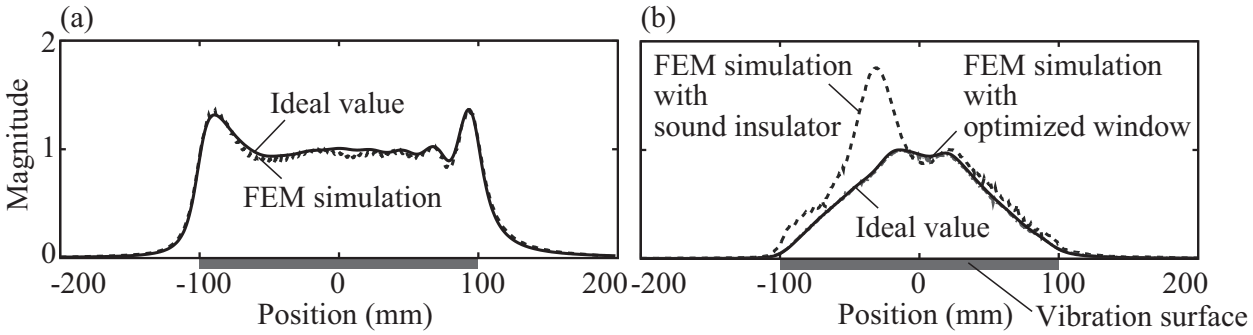


Figure 4.20: Distribution of the particle velocity at the distance 1 mm from the sound insulator ($z$ = 9.96 mm) in $f$ = 6 kHz (a) without sound insulator and (b) with sound insulator.

while considering the physical properties and insulation characteristics of the sound insulator as a future work.

## 4.6 Summary

A planar acoustic transducer generating the evanescent sound field for near-field acoustic communication was proposed. An attempt was made to generate the evanescent sound field with large sound pressure level in audio frequency so that mobile devices equipped with microphones can receive the acoustic data sufficiently. The distribution of sound pressure level of the sound field above the acoustic transducer was measured in a simulation and an experiment. The obtained results suggest that the proposed acoustic transducer can generate the evanescent wave because amplitude of sound pressure was attenuated exponentially. It was clarified that acoustic data can be received near the plate by mobile device since sound is generated with uniform level and small time delay. In addition, a method of suppressing sound leakage to the far field of a near-field acoustic communication system using an evanescent sound field was proposed. A sound wave radiates over an evanescent sound field because of the broadening of the wavenumber spectrum caused by the presence of a discontinuity in the particle velocity. Therefore, in order to suppress sound leakage, we calculated an optimum window function applying to the particle velocity field near a vibrating plate. We investigated a suitable method for calculating the sound pressure level at the far field, and the sound pressure level at the far field with respect to the frequency was calculated for different window shapes. A window function in which the maximum sound pressure level at the far field has the smallest value in the frequency band $1 \leq f \leq 10$ kHz was obtained, and it was defined as the optimized window function. It was confirmed that the optimized window function can limit the area in which acoustic data is transmitted while securing high sound pressure level near the vibrating plate. Additionally, it was found by simulation using the three-dimensional FEM that sound leakage can be suppressed by placing a sound insulator, which has a spatially-weighted shape as the optimized window, above the vibrating surface. Therefore, the applicability of near-field acoustic communication system using the proposed acoustic transducer was indicated.

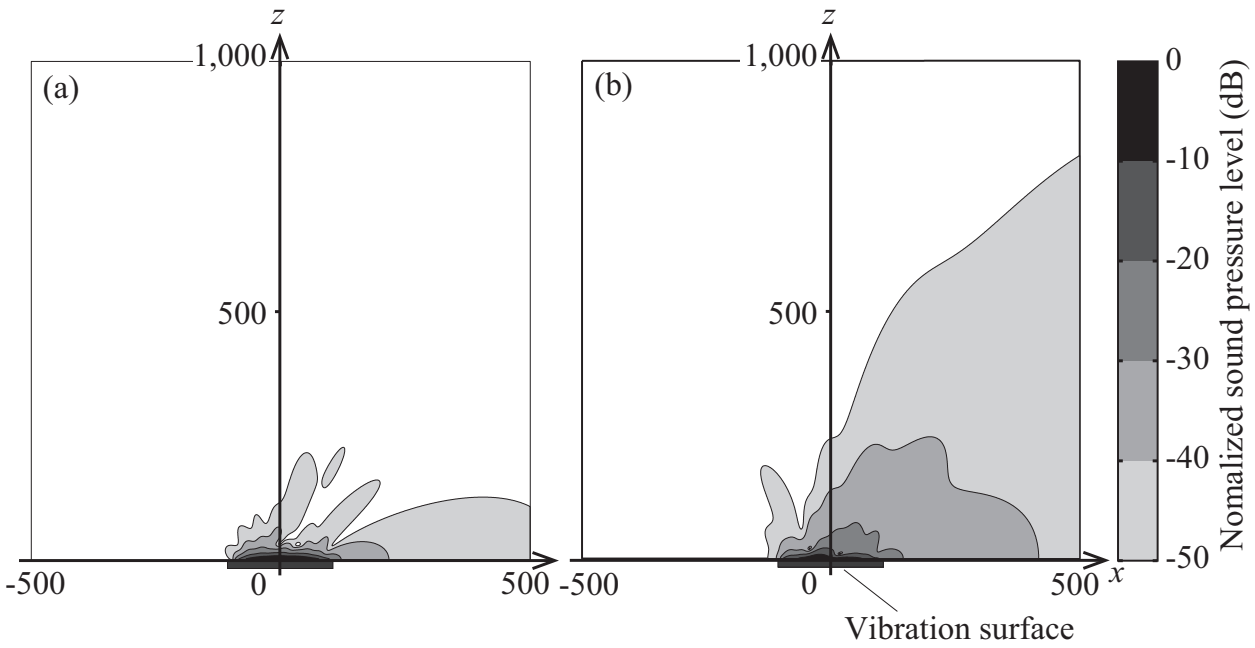


Figure 4.21: Distribution of sound pressure level on the $xz$-plane when $f = 6$ kHz (a) with optimized window (b) with sound insulator.

# Chapter 5

# Conclusions

This paper aimed to analyze the characteristics of the flexural wave and the acoustic fields generated by the flexural wave for creation of objective applications. The dispersion of the phase velocity of the flexural wave is different between the homogeneous panel and the sandwich panel. Therefore, the calculation method to analyze the characteristics of the flexural wave propagating on the panel, especially of sandwiched structure, was proposed. In addition, the feasibility of the applications using the inclined plane wave and the evanescent sound field was estimated.

In chapter 2, the frequency characteristics of the phase velocity of the flexural wave propagating on homogeneous panel and honeycomb sandwich panel were analyzed. First, the propagation characteristics of the elastic wave, especially Lamb wave, was explained in section 2.1. Next, the motion equation of a beam was indicated as the theoretical equation for the homogeneous panel in section 2.2. The phase velocity of the flexural wave was measured using a planar transducer that consists of the acrylic plastic and the piezoelectric transducer, and compared to the theoretical value. It was confirmed that the experimental values were in good agreement with the theoretical values. Finally, the calculation method of the phase velocity of the flexural wave for the honeycomb sandwich panel was proposed in section 2.3. It was suggested that the proposed method was useful to design the honeycomb sandwich panel by comparison among the theoretical value, simulated value, and the experimental value. The vibration panel for the application using the acoustic fields can be designed by calculating the condition under which the evanescent sound field or the inclined plane wave is generated.

In chapter 3, a flat panel loudspeaker using inclined plane wave for generating guiding sound was proposed. First, the demand of the audio guidance system and the problem of existing system was mentioned in section 3.1. Next, the principle of generating inclined plane wave by the flexural wave was indicated in section 3.2. Using the proposed calculation method in section 2.3, the honeycomb sandwich panel for generating inclined plane wave was designed in section 3.3. The sound radiation from the designed panel was simulated using FEM. It was confirmed that the characteristic of radiating sound with uniform angle is useful for indicating the direction of the destination. The obtained results suggested that the proposed loudspeaker using a honeycomb sandwich panel is suitable for audio guidance systems.

In chapter 4, a planar acoustic transducer generating the evanescent sound field for near-field acoustic communication was proposed. First, the background of the near-field communication system and the ex-

isting application using the evanescent sound field was mentioned in section 4.1. Next, generation of the evanescent sound field was confirmed by FEM simulation and the experiment in section 4.2. The communication quality of the proposed acoustic transducer was estimated in section 4.3. It was clarified that acoustic data can be received near the plate by mobile device since sound is generated with uniform level from all over the surface and small time delay. However, it was found that a sound wave leaks slightly over an evanescent sound field because of the broadening of the wavenumber spectrum caused by the presence of a discontinuity in the particle velocity distribution. Therefore, we calculated an optimal window function, which performs spatially-weighting the particle velocity field near a vibrating plate, in order to suppress sound leakage in section 4.4. We investigated a suitable method for calculating the sound pressure level at the far field, and the sound pressure level at the far field with respect to the frequency was calculated for different window shapes. It was confirmed that the optimized window function can limit the area in which acoustic data is transmitted while securing high sound pressure level near the vibrating plate. In addition, suppression of sound leakage was attempted using a porous material, which has a spatially-weighted shape as the optimized window applying to the vibrating surface. The leaking sound was suppressed using sound insulator made of the porous material in FEM simulation in section 4.5. Therefore, the applicability of near-field acoustic communication system using the proposed acoustic transducer was indicated.

As stated above, the calculation method of the flexural wave propagating on the flat panel and the application using generated sound field was proposed. In the field of the audio guidance system, the proposed loudspeaker using inclined plane wave is effective in indicating the direction of the destination exactly. Therefore, the proposed guiding system is expected to guide the pedestrian smoothly and safely in case of emergency. In the field of the near-field acoustic communication system, it was clarified that acoustic data can be received near the plate by mobile device. Thus, the proposed communication system can be utilized as a new communication tool for mobile devices. In addition, these results provides the valuable knowledge for the multiple areas of analyzing and utilizing of the flexural wave and its sound field.

# Acknowledgements

I was bestowed upon Associate Professor Naoto Wakatsuki of the University of Tsukuba, who is my supervisor, a number of valuable advices and technical discussions. He gave long-term support since I entered the university. I have learned from him that it is important to be interested in everything and consider questions in all its aspects deeply in order to acquire knowledge and skill. It was encouraging that he is always close to the students and he discusses with us patiently. Without his guidance and persistent help this thesis would not have been possible. Moreover, my early graduation would not have been achieved without his enormous and continuing help. I owe my deepest gratitude to Associate Professor Naoto Wakatsuki here, I thank from the bottom of my heart.

I greatly appreciate Professor Koichi Mizutani of the University of Tsukuba, for the opportunities and environments to conduct the engineering research. He warmly welcomed me when I visited to the laboratory in my first year of college. I have learned from him that attractive ideas are everywhere and I have to observe ordinaries of everyday life carefully to find that. Furthermore, I always feel his thoughtful consideration and sincere encouragement to every students. I would like to offer my special thanks to Professor Koichi Mizutani from my heart.

I am particularly grateful to Assistant professor Tadashi Ebihara of the University of Tsukuba, for lots of advices and discussions. His meticulous comments were an enormous help to me especially when I presented papers on the results of my studies in English. I would like to show my appreciation to Assistant Professor Tadashi Ebihara deeply.

I would like to thank Keiichi Zempo and Yuka Maeda, Assistant Professors of the University of Tsukuba, for the fruitful advices. Because we are close in age, I could feel free to talk not only about the studies but also about casual events. I thank Keiichi Zempo and Yuka Maeda greatly.

I sincerely appreciate Professor Hiroshi Yabuno of the University of Tsukuba and Professor Masahide Itoh of the University of Tsukuba for their review of my presentations and thesis and their constructive recommendations.

My heartfelt appreciation goes to my beloved sisters, Yuri Nakazawa, Lisa Kosukegawa, and Manami Akiyama, for a lots of amusing conversation and all our yesterdays.

I would like to express my sincere appreciation to fellow in Acoustic Laboratory and all of my friends, especially for Dr. Yoko Norose (currently, Ministry of Defense), Takanobu Kuroyama, Yuki Fujita, Masafumi Aoyanagi, Yusuke Chiba, Masaki Kishi, and Seiya Furukawa for the advices and lots of fun time in the laboratory.

Lastly, I express my heartfelt thanks to my parents, grandmother, and older brother who believe in my potential for the grateful support and consistent encouragement.

# Bibliography


1) D. C. Worlton, Symposium on Nondestructive Test in the Field of Nuclear Energy, ASTM, Special Publication, 1958, **223** p. 260.

2) D. C. Gazis, J. Acoust. Soc. Am. **31**, 568 (1959).

3) D. N. Alleyne and P. Cawley, NDT & E International, 1992, **25**, p. 11.

4) C. T. Ng and M. Veidt, Smart Mater. Struct. **18**, 074006 (2009).

5) H. Lamb, Proc. the Royal Society of London. Series A, Containing Papers of a Mathematical and Physical Character, 1917, **93** (648) p. 114.

6) I. A. Viktorov, *Rayleigh and Lamb Waves* (Plenum Press, New York, 1970) p. 67.

7) D. E. Chimenti and R. W. Martin, Ultrasonics **29**, 13 (1991).

8) S. Ueha, Y. Hashimoto, and Y. Koike, Ultrasonics **38**, 26 (2000).

9) K. Suzuki, K. Han, S. Okano, J. Soejima, and Y. Koike, Jpn. J. Appl. Phys. **48**, 07GM05 (2009).

10) S. H. Ko and C. H. Sherman, J. Acoust. Soc. Am. **62**(2), 566 (1979).

11) E. Kretschmann, Opt. Commun. **5**, 331 (1972).

12) W. Denk and D. W. Pohl, J. Vac. Sci. Technol. B **9**, 510 (1991).

13) D. Axelrod, J. Cell Biol. **89**, 141 (1981).

14) E. Kretschmann, Opt. Commun. **6**, 185 (1972).

15) E. G. Williams and J. D. Maynard, Phys. Rev. Lett. **45**, 554 (1980).

16) E. G. Williams, J. D. Maynard, and E. Skudrzyk, J. Acoust. Soc. Am. **68**, 340 (1980).

17) J. D. Maynard, E. G. Williams, and Y. Lee, J. Acoust. Soc. Am. **78**, 1395 (1985).

18) D. H. Trivett, L. D. Luker, S. Petrie, A. L. Van Buren, and J. E. Blue, J. Acoust. Soc. Am. **87**, 2535 (1990).

19) K. Nakamura and S. Hongo, Jpn. J. Appl. Phys. **37**, 2853 (1998).

20) K. Yamada, D. Yamazaki and K. Nakamura, Jpn. J. Appl. Phys. **43**, 2996 (2004).

21) H. Ito, K. Furuya, Y. Haneda: Proc. IEEE Int. Conf. Acoustics, Speech and Signal Processing, 2012, p.221.

22) F. Song, G. L. Huang, and K. Hudson: Smart Mater. Struct. **18** (2009) 125007.

23) S. M. H. Hosseini and U. Gabbert: Proc. Appl. Math. Mech. **10** (2010) 11.

24) A. Fujii, N. Wakatsuki, and K. Mizutani, Jpn. J. Appl. Phys. **54**, 07HB08 (2015).

25) A. Fujii, N. Wakatsuki, and K. Mizutani, Proc. 20th Int. Congr. Sound and Vibration, 2013, R25-344.

26) A. Fujii, N. Wakatsuki, and K. Mizutani, Jpn. J. Appl. Phys. **53**, 07KB07 (2014).

27) A. Fujii, N. Wakatsuki, and K. Mizutani, Jpn. J. Appl. Phys. **55**, 017301 (2016).

28) R. B. Thompson, G. A. Alers, D. O. Thompson, and M. A. Tennision, J. Acoust. Soc. Am. **57**, 1119 (1975).

29) N. Ogasawara, M. Shiratori, Q. Yu, and A. Miyano, JSME Int. J. **42**, 381 (1999).

30) N. Wakatsuki, S. Wada, Y. Kagawa, and M. Hada, Int. Symp. Inverse Problems in Engineering Mechanics, 2003, p. 58.

31) J. Tardieu, P. Susini, F. Poisson, H. Kawakami, and S. McAdams, Appl. Acoust. **70**, 1183 (2009).

32) J. C. Steinberg and W. B. Snow, SMPTE Motion Imaging J. **61**, 420 (1953).

33) M. Ohuchi, Y. Iwaya, Y. Suzuki, and T. Munekata, Acoust. Sci. Technol. **27**, 5 (2006).

34) T. Fujikawa and S. Aoki, Proc. Meet. Acoust. **19**, 030055 (2013).

35) H. Haas: J. Audio Eng. Soc. Am. **46**, 339 (1969).

36) N. H. Fletcher and T. D. Rossing, *The Physics of Musical Instruments* (Springer, New York, 1998) p. 171.

37) G. Madlmayr, J. Langer, C. Kantner, and J. Scharinger, IEEE 3rd Int. Conf. Availability, Reliability and Security, 2008, p. 642.

38) J. Ondrus and Y. Pigneur, IEEE 6th Int. Conf. Management of Mobile Business, 2007, p. 43.

39) J. Cho, K. Min, and S. Kim, IEICE Trans. Commun. E89-B, 598 (2006).

40) H. Matsuoka, Y. Nakashima, and T. Yoshimura: *Advances in Multimedia Modeling* (Springer, Heidelberg, 2008) p. 498.

41) N. Shinmen, T. Ebihara, and K. Mizutani: Proc. IEEE Global Conf. on Cosumer Electronics, 2012, 152.

42) R. D. Isaak, J. Acoust. Soc. Am. **28**, 556 (1956).

43) M. Stojanovic, J. Catipovic, and J. G. Proakis, J. Acoust. Soc. Am. **94**, 1621 (1993)

44) K. Mizutani, T. Ebihara, N. Wakatsuki, and K. Mizutani: Jpn. J. Appl. Phys. **46** (2007) 4541.

45) K. Mizutani, T. Ebihara, N. Wakatsuki, and K. Mizutani: Jpn. J. Appl. Phys. **47** (2008) 6526.

46) H. P. E. Stern and S. A. Mahmoud, *Communication Systems* (Prentice Hall, New York, 2003) p. 283.

47) G. R. Harris, J. Acoust. Soc. Am. **70**, 10 (1981)

48) J. W. Goodman, *Introduction to Fourier Optics* (McGraw-Hill, New York, 1996) p. 73.

49) M. E. Delany and E. N. Bazley, Appl. Acoust. **3**, 105 (1970).

50) Y. Miki, J. Acoust. Soc. Jpn. (E) **11**, 1 (1990).

# Publication List

## Reviewed journal paper

**(J-1)** A. Fujii, N. Wakatsuki, and K. Mizutani, Jpn. J. Appl. Phys. **53**, 07KB07 (2014).

**(J-2)** A. Fujii, N. Wakatsuki, and K. Mizutani, Jpn. J. Appl. Phys. **54**, 07HB08 (2015).

**(J-3)** A. Fujii, N. Wakatsuki, and K. Mizutani, Jpn. J. Appl. Phys. **55**, 017301 (2016).

## Reviewed international conference paper

**(P-1)** A. Fujii, N. Wakatsuki, and K. Mizutani, Proc. 20th Int. Cong. Sound and Vibration, 2013, R25-344.

## Proceedings of conferences

**(1)** A. Fujii, N. Wakatsuki, and K. Mizutani, Proc. Musical Acoustics of Acoust. Soc. Jpn., **31**, No. 3, 2012, p.1 (in Japanese).

**(2)** A. Fujii, N. Wakatsuki, and K. Mizutani, Proc. the 9th IEEE Tokyo Young Researchers Workshop, **47**, 2012 p.42.

**(3)** A. Fujii, N. Wakatsuki, and K. Mizutani, Proc. Acoust. Soc. Jpn. (2013 Autumn Meet.), 2013, p. 1243 (in Japanese).

**(4)** A. Fujii, N. Wakatsuki, and K. Mizutani, Proc. the 10th IEEE Tokyo Yong Researchers Workshop, **64**, 2013, p. 50.

**(5)** A. Fujii, N. Wakatsuki, and K. Mizutani, Proc. the 34th Symposium on Ultrasonic Electronics, 2013, p. 421.

**(6)** A. Fujii, N. Wakatsuki, and K. Mizutani, Proc. the 35th Symposium on Ultrasonic Electronics, 2014, p. 403.

**(7)** A. Fujii, N. Wakatsuki, and K. Mizutani, Proc. SAT Technology showcase 2015, p.84. (in Japanese)

**(8)** A. Fujii, N. Wakatsuki, and K. Mizutani, Proc. the 36th Symposium on Ultrasonic Electronics, 2015, 1P1-1.

## Unrelated to this paper

**(1)** A. Fujii, N. Wakatsuki, and K. Mizutani, Proc. Musical Acoustics of Acoust. Soc. Jpn., **30**, No. 8, 2012, p.7 (in Japanese).